North Carolina Agricultural and Technical State University

Aggie Digital Collections and Scholarship

2012

Characterization Of Coated Aluminum Particles For Combustion And Ignition Studies

Amanda Michele Breeden
North Carolina Agricultural and Technical State University

Follow this and additional works at: https://digital.library.ncat.edu/theses

Recommended Citation

CHARACTERIZATION OF COATED ALUMINUM PARTICLES FOR
COMBUSTION AND IGNITION STUDIES

by

Amanda Michele Breeden

A thesis submitted to the graduate faculty
in partial fulfillment of the requirements for the degree of
MASTER OF SCIENCE

Department: Mechanical Engineering
Major: Mechanical Engineering
Major Professor: Dr. S. Owusu-Ofori

North Carolina A&T State University
Greensboro, North Carolina
2012

School of Graduate Studies
North Carolina Agricultural and Technical State University

This is to certify that the Master's Thesis of

Amanda Michele Breeden

has met the thesis requirements of
North Carolina Agricultural and Technical State University

Greensboro, North Carolina
2012

Approved by:

_____   _____
Samuel Owusu-Ofori   Dhananjay Kumar
Major Professor   Committee Member

_____   _____
John Kizito   Samuel Owusu-Ofori
Committee Member   Department Chairperson

_____
Sanjiv Sarin
Associate Vice Chancellor for Research
and Graduate Dean

ii

DEDICATION

This thesis is dedicated to my family: my mother (Lynda Breeden), father (Roland Breeden), and sister (Angela Breeden). Their support and endless words of encouragement have been invaluable throughout my academic career.

BIOGRAPHICAL SKETCH

Amanda Michele Breeden was born on May 14th, 1988, in Winston-Salem, North Carolina. She graduated from North Forsyth High School located in Winston-Salem, NC in June 2006. She completed her Bachelor of Science degree in Mechanical Engineering on August 1st, 2010, from North Carolina A&T State University in Greensboro, NC. She has studied the coating process and surface morphology of aluminum particles coated with magnesium and nickel for studies in combustion characteristics of these coated aluminum particles. She is a candidate for the Master of Science degree in Mechanical Engineering.

ACKNOWLEDGMENTS

TABLE OF CONTENTS

LIST OF FIGURES

LIST OF TABLES

ABSTRACT

Breeden, Amanda Michele. CHARACTERIZATION OF COATED ALUMINUM PARTICLES FOR COMBUSTION AND IGNITION STUDIES. (Major Advisor: Samuel Owusu-Ofori), North Carolina Agricultural and Technical State University.

The goal of the research was to contribute to the knowledge of the characteristics of aluminum particles used for thermobaric weapons (TBX). It was desired to continue the research efforts conducted to produce an effective coating process to improve the reactivity of aluminum flakes. This was done by coating the particles with magnesium and nickel in a modified Pulsed Laser Deposition (PLD) system. The effects of the laser deposition on the morphology and surface chemistry of the aluminum particles were studied.

In this research, modifications were made to a PLD system and experiments conducted to determine the coating effectiveness of Magnesium (Mg) and Nickel (Ni) on aluminum flakes and spherical particles. The experiments were conducted in a ~10^{-5} Torr pressure environment. Scanning Electron Microscopy (SEM) was used to capture images of the surface profile of particles from each sample. Comparative results from the SEM images indicated that both Mg and Ni were successfully deposited on the aluminum particles. The challenge was to obtain consistent coating over the surface of the particles. Additionally, the particles that received extended exposure to the target plume did not show significant increase in film growth. The results of this research demonstrate that the modified PLD system was able to effectively deposit a thin-film layer of metallic material onto aluminum particles but did not produce uniform surface characteristics.

CHAPTER 1

INTRODUCTION

As the war on terrorism unfolded in countries throughout the world, the U.S. government formed several research agencies and heightened national security in an effort to lessen the effects of weapons of mass destruction (WMD) on the population. The Defense Threat Reduction Agency (DTRA) was tasked with obtaining and studying possible WMDs in efforts to mitigate their effects which could be in the form of chemical, biological, nuclear, radiological or high-explosive devices [DTRA, 2008]. Thermobaric weapons are highly explosive weapons that draw in atmospheric oxygen for ignition. Superior to conventional explosives, thermobaric weapons produce increased explosive energy and are more effective in confined spaces such as bunkers and missile silos. These weapons use a combination of heat and pressure to cause destruction. This research sought to investigate the changes in surface and chemical morphology caused by coating these aluminum particles with energetic materials.

1.1   Thermobaric Weapons

Until the 1960s, conventional detonation penetration devices were the weapons of choice for military strikes during war conflicts. During the Cold War, the former Soviet Union became one of the first nations to use thermobaric weapons. These devices rapidly release energy in the form of a blast wave and shattering of the bomb casing inflicting injury to victims. Thermobaric weapons are typically filled with a solid fuel

monopropellant and energetic particles such as powdered aluminum [Dorneanu, 2007]. In recent years, thermobaric bombs have been developed to encompass flammable particles which create a fireball and shock wave when ignited. Atmospheric oxygen is removed from all surrounding areas following the fire. Figure 1.1 illustrates the sequence of events after a thermobaric bomb strikes an underground tunnel. The multi-stage explosion has the ability to penetrate beyond the surface and inflict damage to equipment and individuals in hidden places.
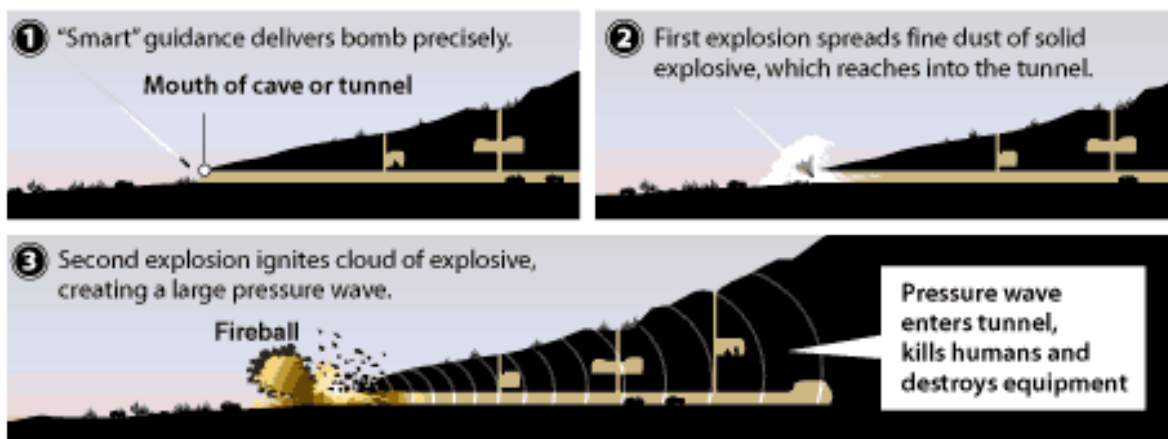
Figure 1.1 Thermobaric bomb attack on underground tunnel [Marcus, 2002]

The combustion of these weapons is comprised of exothermic chemical reactions between fuel and an oxidant producing heat and light. Gaseous, liquid, or solid fuels can be utilized as a heat source for the ignition.

1.1.1 Ramifications of Thermobaric Weapons

Thermobaric weapons are effective for clearing desired targets but the wide striking range (>300 meter radius) often leads to unintentional civilian deaths. The

proximity of the victims to the initial blast plays a major factor into the sequence of harmful effects. Figure 1.2 depicts the cause of injury in terms of the radial distance from the impact of a thermobaric weapon. The initial threat from thermobaric bombs is the high temperature fire that is created upon ignition of the flammable particles. This causes the ignition of any garments or equipment located on or near the victim. Secondly, a victim would likely suffer from blunt force trauma and asphyxiation as a result of invisible shock waves and removal of atmospheric oxygen, respectively.

Figure 1.2 Injuries caused by thermobaric weapons in terms of radius from impact [Wildegger-Gaissmaier, 2003]

1.1.2 *Energetic Materials in Thermodynamics*

Energetic materials date back to the eleventh century with the discovery of gunpowder and have evolved to include various physical forms. Energetic materials are characterized by their ability to store and discharge a vast amount of energy in the form of shock waves and exceedingly high temperatures. The ability to increase the destructive force has made aluminum powders one of the more common energetic fuel additives. The melting point of the aluminum oxide shell is approximately 2327 K and correlates to the ignition temperature. Studies have shown that the ignition delay of Al particles is dependent on the oxide shell thickness [Beckstead, 2005]. Experiments have been conducted in recent years to study the effects of applying a thin-layer of magnesium or nickel to the surface of aluminum particles to slow the occurrence of oxidation and decrease the temperature required to ignite the aluminum particles.

1.2   Research Motivation

Research previously conducted by M. Ellis [2010] served as a precursor to this work. The coating methods developed by Ellis proved to be ineffective for coating the aluminum flakes. Several modifications to the pulsed laser deposition process were made to accommodate coating multiples sides of the particles. During his efforts, he was unable to identify a method to control the film growth or attain the desired surface characteristics. This research focuses on the characterization of the coated surface to determine its morphology prior to the ignition experiments.

The ignition and combustion studies were conducted in a modified Hencken flat flame burner which did not accurately replicate the environment that would cause these coated particles to react in the field. For these reasons, it was desired to make further modifications to the coating process in efforts to attain better surface and morphology characteristics as well as conduct combustion experiments in a high pressure, high temperature environment.

The ballistic compressor facility at The Pennsylvania State University was considered to study and characterize the ignition and combustion energetic fuel particles. This system was instrumented with a test section that would allow for the ignition and burning processes of energetic fuel particles to be observed. Theoretically, the ballistic compressor would operate at high pressures (> 100 kpsi) and heating rates greater than 10^6 K/s with a selectable gas composition to simulate the conditions found in a detonation such as that of thermobaric explosives (TBX) [Kuo et al, 2010]. Data gathered from these experiments could provide insightful information on the combustion of energetic particles in high pressure conditions.

1.3   Research Objectives

The goal of this research was to improve the reactivity of aluminum particles using magnesium and nickel. It was necessary to make minor improvements to the previously modified Pulsed Laser Deposition to achieve desirable results. The effects of the coating on the morphology and surface chemistry were studied using Scanning

Electron Microscopy and Energy Dispersive Spectroscopy. Additionally, a baseline for future ignition and combustion experiments using a ballistic compressor was studied. Specific objectives were:

1. Modify the experimental setup of the Pulsed Laser Deposition system to effectively deposit nickel and magnesium onto 32µm aluminum particles.

2. Evaluate particle movement using various sized particle holders with the vibratory system previously established.

3. Characterize the morphology of the coated surface.

1.4   Thesis Outline

Chapter 2 provides an overview of preliminary studies and findings pertinent to this research. Specifications for ignition and combustion studies utilizing the ballistic compressor at The Pennsylvania State University are also discussed. Chapter 3 presents the experimental setup and equipment used for characterization used in this study. The experimental results were presented in Chapter 4. Conclusions are made in Chapter 5 along with details about future recommendations for this work.

CHAPTER 2

LITERATURE REVIEW

This chapter focuses the background information necessary to understand the processes and methods chosen in this research. It encompassed the specifications for the various coating methods, the characterization methods, and the aluminum particle combustion evaluation.

2.1 Energetic Materials

2.1.1 Aluminum Characteristics

Aluminum has been used as an energy source for over 50 years. Various applications include the use as an additive for solid propellants and as a primary fuel in composite propellants [Sutton, 2010]. Utilization of aluminum is advantageous to thermobaric weapons (TBX) due to the particles being highly explosive in the fine dust form. One of the disadvantages of using aluminum is the rapid oxidation of the surface when exposed to the atmosphere. The thickness of the oxide layer affects the ignition temperature and characteristics of the aluminum particles.

Ellis [2010] previously discussed the advantages of using aluminum flakes over spherical particles, stating the flakes had a higher aluminum content that the spheres. Most notably, the lesser cost of aluminum flakes was the leading factor for using flakes over the more commonly used aluminum spherical particles [Ellis, 2010]. The results of his research indicated subpar surface characteristics after the deposition process. For this

reason, the use of aluminum spheres was considered to determine if the geometry had an effect on the coating process.

The aluminum particle flakes used for this research were 16μm x 200nm SilBerCote^{TM} PC 8602 X, manufactured by Silberline ® Corporation, which is located in Tamaqua, PA. These particles are covered with a thin layer of proprietary inorganic material which prevents oxidation and potentially harmful dust clouds, without affecting the reaction of the aluminum particles [Houim, Boyd, and Kuo, 2008]. The aluminum spherical particles used were 32μm in size supplied by Technion of Israel via the HPCL at Penn State University.

2.1.2   Coating Elements

Aluminum particles are often chosen for TBX due to their ability to release great amounts of energy, however they are also difficult to ignite. Introducing a coating to the particle surface was proposed in prior studies to help facilitate ignition. This research effort utilized magnesium and nickel as coating elements to create thin films on the aluminum particles. Several studies have found these materials to have desirable explosive characteristics.

A study by Yagodnikov and Voronetskii [1997] on an aerosolized cloud of Ni-coated aluminum particles found the flame propagation rate to be 1.5 to 4.0 times faster than uncoated particles [Yagodnikov & Voronetskii, 1997]. Nickel a reactive material with notable hardness and ductility. The melting temperature of nickel is 1723K while the alumina outer shell melts at 2327K. This temperature difference could explain why the ignition temperature of an aluminum particle would be reduced if coated with nickel.

Nickel's inertness to oxidation made it a likely material to compare to magnesium that develops an oxide layer in atmospheric pressure. Studies using Ni-coated aluminum particles with less that 25% wt nickel have been inconclusive about the reactivity in inert atmospheres which is a disadvantage to the coating process developed in this research.

Magnesium was also considered for its high flammability and formability. It effortlessly ignites when in the form of thin strips, films or powder. Magnesium is most notably used in fireworks and military flares. Studies have shown Magnesium to reach flame temperatures of approximately 3300 K [Dreizin et al., 2000]. The low mass of magnesium is also attractive for transportation of TBX bombs [Fournier et al., 2001]. The rapid oxidation of the Mg coated aluminum particles is a disadvantage in using magnesium. Due to the type of process used in this research, prevention of the oxidation is very hard to achieve. The $Mg(OH)_2$ layer of magnesium does not have positive corrosive characteristics thus Mg products are typically treated with an anti-corrosive coating if they will be exposed to outdoor environments [Fournier et al., 2001]. The characteristics associated with ablating these materials are shown in Table 2.1. The values are important when considering deposition of the materials.

Table 2.1 Evaporative Characteristics of Materials

Material	Minimum Evaporative Temperature (°C)	State of Evaporation	Deposition Rate (Å/s)	Power (kW) (e-beam[b])
Magnesium	327	Sublimes	100	0.04
Nickel	1262	Melts	25	2

2.1.3 Particle Coating Methods

The process of coating particles to achieve desired characteristics has been studied in academic research for several decades. The continual advancements have fueled on the increasing number of coating methods as seen in Table 2.2. Of these methods, chemical vapor deposition (CVD) has received significant research acknowledgment for its ability to produce high quality thin films on hard surfaces. CVD is dependent on the availability of a volatile chemical which can be converted by a reaction into the desired solid film [TimeDomain CVD, 2002].

Chemical Vapor Deposition is most commonly used to grow thin crystalline structures. The growth of these structures is characterized by the two forms of epitaxial growth namely, homoepitaxy and heteroepitaxy. The better quality crystalline structures are made with homoepitaxy in which the lattice matrix is the same material as the substrate, for example Ni lattice on Ni substrate. Heteroepitaxy occurs when the lattice is different from that of the substrate.

Table 2.2 Requirements and Performance of Deposition Techniques

Technique	Energy Range (eV)	Vacuum Requirement	Multi-Element Control	Background Gas
Thermal Evaporation	0.1	HV	Difficult	No
(Accelerated) Molecular Beam Expitaxy	0.1 / 0.1 – 100	UHV	Moderate	No
Cathodic Arc	0.1 – 1000	HV	Moderate	Yes
Chemical Vapor Deposition	0.1 / 0.1 – 500	HV	Moderate	Yes
Suttering	1 – 1000	HV	Easy	No
Ion Beam Deposition	50 – 1000	UHV	Difficult	No
Pulsed Laser Deposition	1 – 1000	HV	Easy	Yes

In earlier studies, the surface characteristics and film quality when using CVD were found to be superior and preferred over other methods such as pulsed laser deposition. The disadvantages to CVD include the complexity of the process, extreme toxicity and flammability of the chemicals involved in the process and expensive environmental disposal cost [TimeDomain CVD, 2002].

The method of deposition located at the Center for Advanced Materials and Smart Structures (CAMSS) was pulsed laser deposition (PLD). This technique was chosen for the ease of operation and ability to modify the chamber without inhibiting operation. To better understand the operation and function of the PLD, pertinent background information was needed.

Shortly after the development of the first laser in 1960, laser-assisted film growth was used to deposit the first thin films in 1965. These preliminary depositions did not produce samples with the same quality produced by chemical vapor deposition (CVD) or molecular beam epitaxy (MBE). A breakthrough in the development of pulsed laser deposition (PLD) was achieved in 1987 when scientists in the former USSR were able to achieve thin film structures with quality superior to other methods. PLD has since evolved with the addition of laser capabilities. Pulsed laser deposition is a broadly applicable technique for thin-film deposition research. Deposition of solid metals, polymers, and biological materials are some of the many uses of PLD.

Pulsed laser deposition is a four step deposition process consisting of: laser ablation, plasma expansion, deposition of the material and growth of the film. Part of the bulk target material is removed from the target by a complicated process of electron

energizing and vaporization. Secondly, the material expands in a plasma plume towards the substrate. The distribution of the plume is dependent on the chamber pressure. This step is essential to producing high quality deposited films. If ablated atoms reflect off of the substrate, damage may result decreasing the quality of the deposition. Lastly, the deposited particles can grow into a thin film by three growth methods detailed below.

Studies conducted by Hertz in 1882 on evaporation rates indicated that the rates were proportional to the difference between the equilibrium pressure of mercury and the hydrostatic pressure acting on an evaporant [Ohring, 2002]. It was concluded that the rate of evaporation from both liquid and solid surfaces maybe presented as

$$\phi_e = \frac{\alpha e \, N_A (P_e - P_h)}{\sqrt{2\pi MRT}} \tag{2.1}$$

where ϕ_e is the evaporation flux in number of atoms (or molecules) per unit area, per unit time, and α_e is the coefficient of evaporation ($0 \leq \alpha_e \leq 1$). P_e and P_h are the equilibrium pressure and the hydrostatic pressure, respectively. Maximum evaporation rate is realized when $\alpha_e = 1$ and P_h is zero [Ohring, 2002].

The laser is a vital part of the pulsed laser deposition method. The most common gas excimer lasers are ArF (193 nm), KrF (248 nm), and XeCl (308 nm) types. The intensity of the high-power laser beam serves as the evaporation source intense enough to vaporize the hardest and most heat resistant materials. In scientific research, lasers are attractive for their high precision and reliability.

The laser box is positioned outside the vacuum deposition chamber and focused on the target by means of external lenses. The absorbed beam energy is converted into thermal, chemical and mechanical energy to ablate and remove atoms from the target

12

surface. Determining the out of energy and intensity required to ablate the target is necessary. The light intensity given off by a laser can be calculated using Beer's law [Ohring, 2002]. Equation 2.2 provides the light intensity at a distance z:

$$I(z) = I_o e^{-\alpha x} \tag{2.2}$$

where α^{-1} is the optical-absorption depth and x is the depth beneath the surface. The distance between the target and how far a pulse of heat spreads with respect to time is derived from Equation 2.3 as the thermal-diffusion distance (D):

$$D = 2\sqrt{\frac{k}{\rho c_p} t} \tag{2.3}$$

A schematic of the inside of a PLD system is presented in Figure 2.4. The lens focuses the laser beam onto the target. The directed laser energy contacts the target and causes the contact point to evaporate.
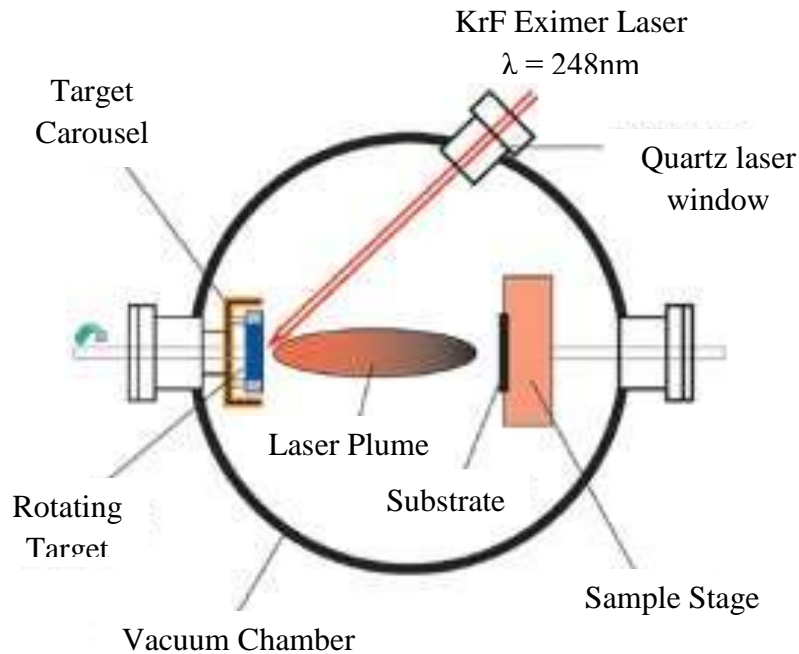
Figure 2.1 Pulsed Laser Deposition Chamber Schematic [Andor Technology, 2010]

13

The quartz windows of the chamber must be able to withstand high pressure conditions ($<10^{-6}$ torr-liters/s) without leaking. They must satisfy the required optical transparency of both visible and ultraviolent light [Ohring, 2002]. The uniformity of the film surface is of great concern when using PLD. The amount of deposited atoms decreases from the inner region of the plume to the outside. The target and substrate are rotated to produce a uniform deposition over a larger region.

2.1.4 Thin-Film Growth

The last step of the PLD process is nucleation and thin-film growth. Nucleation is separated into two classes: homogeneous and heterogeneous nucleation. Several parameters must be considered during this step such as: laser parameters, surface temperature, chamber pressure and substrate surface. Each of these parameters affects the type of film growth that occurs on the substrate surface. A high supersaturation on the substrate surface correlates to the nucleation density, increasing the smoothness of the deposited film [UT-Knoxville, 2011]. Figure 2.2 illustrates the atomic processes in the nucleation atom clusters on the surface of a substrate.

Homogenous nucleation encompasses a vapor to solid state condensation reaction similar to PLD. This results in a reduction of the chemical-free energy of the system. The change in chemical-free energy per unit volume is represented by ΔG_v. ΔG_v can be expressed in terms of the Boltzmann constant, atomic volume, and pressure. Equation 2.4 presents these relationships that govern film growth:

$$\Delta G_v = -\frac{k_B}{\Omega} ln \frac{P_v}{P_s} \qquad (2.4)$$

where P_v and P_s are the supersaturated vapor and vapor pressure above the solid; also, Ω is the atomic volume. This equation follows the notion of energy reduction because ΔG_v is negative and $P_v > P_s$, creating a new surface and interface [Thin film growth].
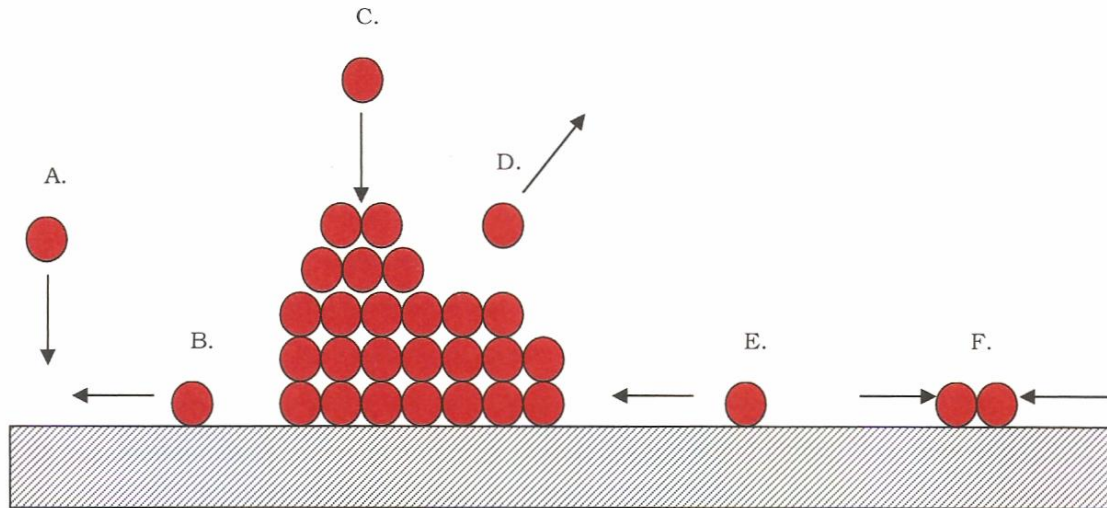
Figure 2.2 Atomic growth processes: (A) absorption or adatom, (B) detachment, (C) deposition, (D) evaporation, (E) diffusion, and (F) nucleation between atoms

A resulting increase in the surface-free energy of the system is related to the geometrical shape of the atoms or molecules. This allows for further manipulation of Equation 2.4 to introduce the solid-vapor interfacial energy per unit area, γ [Ohring, 2002]. The total free-energy change is presented in Equation 2.5. Free energy of nucleation of 2D and 3D are shown in Figure 2.2.

$$\Delta G = \frac{4}{3}\pi r^3 \Delta G_v + 4\pi r^2 \gamma \tag{2.5}$$

The critical free energy and radius are achieved when the derivative of the free energy with respect to the nucleus size is zero ($d\Delta G/dr = 0$). Equation 2.6 is derived when the critical nucleus size $r = r^*$, where

$$r^* = \frac{-2(a_1\gamma_{fv} + a_2\gamma_{fs} - a_3\gamma_{sv})}{3a_3 G_v} \tag{2.6}$$

with geometric constants $a_1 = 2\pi(1 - \cos\theta)$, $a_2 = \pi\sin^2\theta$, and $a_3 = (\pi/3)(2 - 3\cos\theta + \cos^3\theta)$. The critical free energy is defined by Equation 2.7. Figure 2.3 is the graphical illustration of the relationship between the angle θ and γ values known as the wetting angle.

$$\Delta G^* = \frac{16\pi(\gamma_{fv})^3}{3(\Delta G_v)^2}\left[\frac{2 - 3\cos\theta + \cos^3\theta}{4}\right] \tag{2.7}$$

In homogenous nucleation, the geometric constants may become negligible in which r^* is simplified to Equation 2.8. Additionally, Equation 2.9 presents the critical free energy for the simplified case.

$$r^* = \frac{-2\gamma}{\Delta G_v} \tag{2.8}$$

$$\Delta G^* = \frac{16\pi(\gamma_{fv})^3}{3(\Delta G_v)^2} \tag{2.9}$$
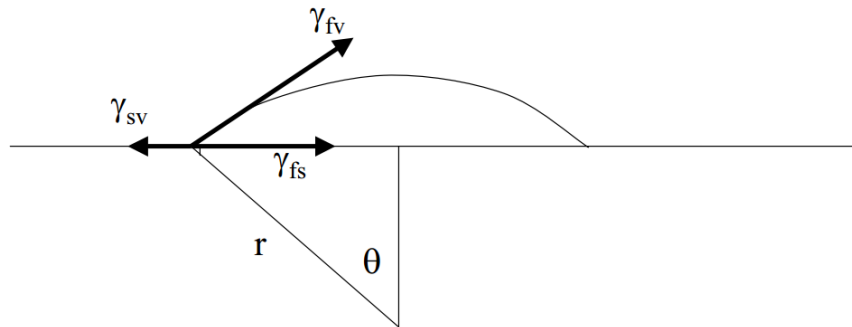
Figure 2.3 Wetting Angle of Heterogeneous Nucleation

The nucleation rate is the next parameter of importance. By lowering ΔG^*, the contact angle is reduced which is evident in the case heterogeneous nucleation. The nucleation rate is then defined as a function of ΔG^* as in Equation 2.10 [Claeyssens, 2001]. Fine-grained or amorphous structures are produced at high nucleation rates produce, while low rates produce coarse-grained deposits.

$$\dot{N} = 2\pi r^* a_0 sin\theta \frac{PN_A}{\sqrt{2\pi MRT}} n_s exp \left(\frac{E_{des} - E_s - \Delta G}{k_B T} \right) \tag{2.10}$$

For the homogeneous cases, $\dot{N}$ is proportionate to ω, the rate of atom impingement on to the surface of the nuclei and the critical area A^* as seen in Equation. 2.11.

$$\dot{N} = n_s exp \left(\frac{-\Delta G^*}{k_B T} \right) A^* \omega \tag{2.11}$$

The most common growth modes describe by Young's Equation are: Volmer-Weber (Island Growth), Frank-van der Merwe (Layer-by-Layer Growth), and Stranski-Krastarov (Mixed Growth). An illustration of these growth modes are presented in Table 2.3. The total surface energy per unit area and the lattice constants of the film and of the substrate determine the growth mode of the film [Chrisey and Hubler, 1994]. Equation 2.12 is the standard equation used to derive the Young's Equation for each growth mode:

$$\gamma_{sv} = \gamma_{fs} + \gamma_{fv} cos\theta \tag{2.12}$$

where θ represents the wetting angle, as demonstrated in Figure 2.2. Equation 2.13 shows the Young's Equation in terms of the wetting angle:

$$cos\theta = \frac{(\gamma_{sv} - \gamma_{fs})}{\gamma_{fv}} \tag{2.13}$$

Table 2.3 Three Growth Modes: Island, Layer by Layer and Mixed Growth Mode

Growth Modes	Young's Equation	Schematic Drawing
Volmer – Weber (Island Growth)	$\gamma_{sv} < \gamma_{fs} + \gamma_{fv}$	
Frank – van der Merwe (Layer by Layer	$\gamma_{sv} \geq \gamma_{fs} + \gamma_{fv}$	
Stranski – Krastarov (Mixed Growth)	$\gamma_{sv} > \gamma_{fs} + \gamma_{fv}$	
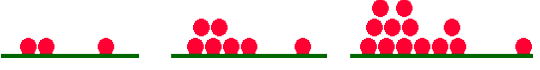
The first growth method discussed is also known as the three-dimensional growth. Volmer-Weber or Island Growth occurs when a cohesive energy imbalance exists between the atoms is and the film. The result is the development of a film layer made from isolated island formations on the surface of a substrate. The islands are formed when metal or semiconductor films are deposited onto oxide substrates with a large supersaturation ($\Delta\mu$).

The Frank-van der Merwe growth mode (Layer-by-Layer Growth) occurs when the nucleus expands in two dimensions forming planar sheets. This is notable means for producing two-dimensional layered structures. Layer-by-layer growth mode has a stronger substrate-to-atom bond than atom. In layer-by-layer growth, the processes occur at undersaturation in contrast to the supersaturation condition of island growth [Liu, 1998].

The third mode is the Stranski-Krastanov growth mode also known as mixed growth. This is due to the combining of layer-by-layer and island growth modes. Several

two-dimensional layers are initially formed until the critical thickness is reached. At this stage island growth begins as a result of the atomic nucleation bond surpassing the bond between the atom and the substrate. A finite supersaturation is required for this nucleation growth mode to be effective.

2.2   Characterization Methods

This section discusses the surface and subsurface characterization methods and how they were implemented.

2.2.1   *Energy Dispersive X-Ray Spectroscopy*

Energy dispersive X-ray spectroscopy uses the interaction of an electron beam with a sample target to separate the characteristic x-rays of different elements into an energy spectrum. EDS has the capability to find the chemical composition of materials measuring a few microns [Goodge, 2012]. EDS detectors are commonly coupled with Scanning Electron Microscopy. This enables users to capture imagery and compositional data using the same sample.

The EDS detector contains a crystal that absorbs the energy of incoming x-rays and converts the x-rays into electrical voltages corresponding to the elemental characteristic x-rays. The x-rays are reflected on an EDS spectrum plot x-ray counts against energy (in keV). Elements with higher composition concentration typically display higher energy peaks. One of the disadvantages to EDS is the overlap of some elements and inability to detect elements with lower elemental abundances. For this reason, wavelength dispersive spectroscopy (WDS) is used for more precise detection.

EDS is still considered a reliable and precise alternative to WDS. A comparison of the characterization methods is presented in Table 2.4.

Table 2.4 Summary of Major Characterization Methods, XPS (X-ray photoelectron spectroscopy), RBS (Rutherford backscattering), and SIMS (Secondary-ion mass spectroscopy)

Method	Elemental Sensitivity	Detection Limit (at. %)	Lateral resolution	Effective probe depth
SEM/EDS	Na – U	~0.1	~1 µm	~1 µm
AES	Li – U	~0.1 – 1	500 Å	15 Å
XPS	Li – U	~0.1 – 1	~100 µm	15 Å
RBS	He – U	~1	1 mm	200 Å
SIMS	H – U	0.001	~1 µm	15 Å

2.2.2   Scanning Electron Microscopy

Scanning Electron Microscopy is a method used to visually characterize the surface of a sample. It is widely utilized to characterize thin films, powders and structures. SEM gradually develops an image in small sections by a scanning probe. In 1935, Max Knoll acquired the very first SEM image of silicon steel. The foundation for the transmission and surface scanning electron microscopy was started in 1937 by Manfred von Ardene and later continued by Charles Oatley and Gary Steward in 1965. A schematic of a SEM electron gun and lenses enclosure is shown in Figure 2.4.

The additional components that comprise the SEM system include a control console, pump and vacuum system, and computer. The computer is used to view and manipulate images as well as run software to control certain functions of the SEM. The control console allows for adjustment of focus, brightness, contrast, magnification, and location of the sample during imaging.
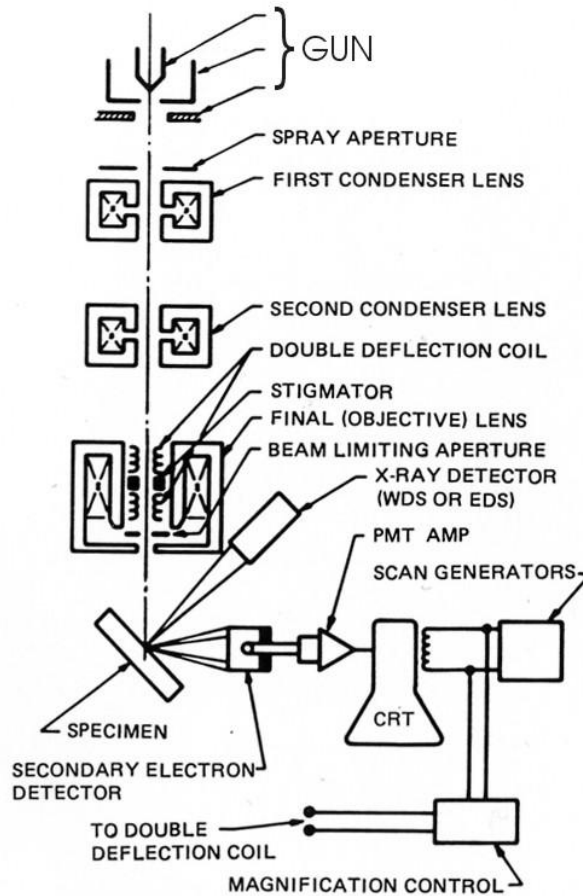
Figure 2.4 Schematic Drawing of electron and X-ray optics

The vacuum system reduces the pressure within chamber and prevents contamination. The SEM system used in this effort was equipped with a turbo vacuum pump that consisted of several axial compressors allowing for the chamber pressure to drop below 10^{-8} torr. The electron gun and lenses enclosure is the most vital component of the SEM system. Directed electrons are used to form the images generated by the electron gun. The electrons are accelerated producing energy ranging from 0.1 to 30 kilo-electron volts (keV) [Goldstein, Echlin, and Joy, 2007].

2.2.3 Auger Electron Spectroscopy

The Auger Electron Spectroscopy (AES) is another method to characterize the elemental composition of surface and subsurface atoms. Its process is similar to SEM/XDS but provides better composition data. Initially based on the discovery of French physicist Pierre Auger, AES measures the energy and intensity of the electron signal emitted from atoms located within 5 to 20Å of a surface. Auger's discovery explained the lack of radiation relaxation of excited atoms [Chourasia and Chopra, 1997]. This phenomenon was initially reported in the journal Zeitschrift für Physik in 1922 by Lise Meitner, but Auger is most commonly credited with the discovery although not reported until 1925.

The components of an AES system are labeled in the schematic shown in Figure 2.5. An ultra-high vacuum (UHV) system is utilized to avoid of contamination of a specimen's surface. Some systems also use an ion gun to ensure any contamination is minimized. Scanning electronics similar to SEM image the surface of the sample. An electron gun focuses a beam of approximately 1.5 to 3 keV electrons at the surface of the specimen. The intensity of the Auger peak above the background of scattered electrons is measured and displayed in the form of an intensity map. The map is correlated to a gray scale with whiter areas indicating higher element concentration.
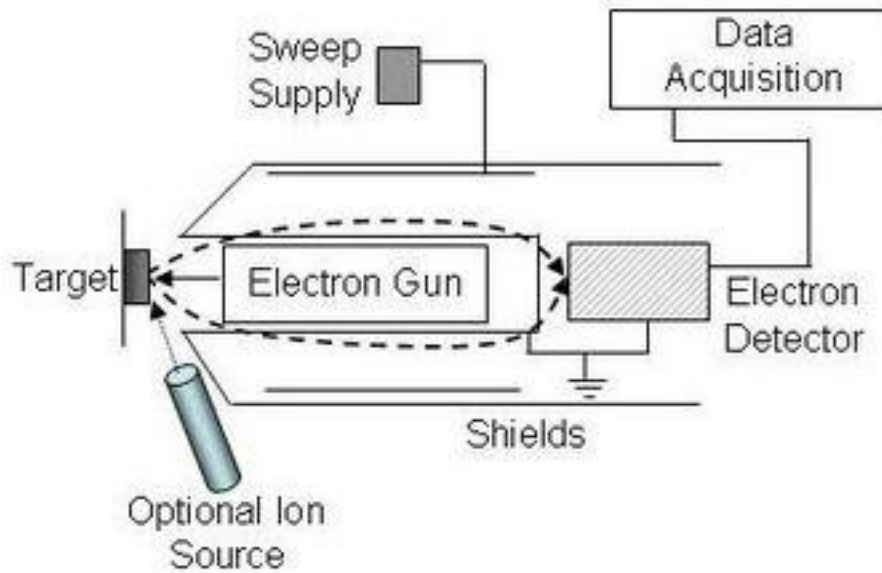
Figure 2.5 Schematic of AES system

The electron quantity detected is plotted against the electron kinetic energy [Chourasia and Chopra, 1997]. The kinetic energy is given by the difference in the binding energies of energy levels A, B and C as in Equation 2.14.

$$E_{ABC}(c) = E_z(z) - E_B(z) - E_C^*(z) \qquad (2.14)$$

For an arbitrary ABC transition of an atom of atomic number, z and φ represents the work function of the analyzer material. In AES, the atomic core levels are ionized by electron beams. An electron spectrometer is used to detect the resulting Auger electrons. The energy displacement of the peaks identifies the elements and the chemical states present. The high sensitivity for chemical elements in the 5 to 20-Å region near the surface, ability to detect all elements other than helium, data acquisition speed, and capability of high-spatial resolution are all advantages of AES.

2.3   Aluminum Particle Combustion

Combustion is described as an exothermic reaction between a fuel and oxidant. In complete combustion reactions the products encompasses compounds formed by the elements of the fuel and oxidant.

2.3.1   Aluminum Combustion

Aluminum particles have been used for many years as fuel and additives in rocket motors. The high energy release is attractive to researchers but the outer layer of alumina makes the element extremely difficult to ignite [Glassman, 1959]. This is a significant issue in the field of thermobarics in which the particles need to ignite at low temperatures.

A comprehensive study conducted by Beckstead [2005] explained the dependency of combustion temperature of aluminum on the thickness of the oxide layer. To quantitatively access the burning time of the aluminum particles, comparisons were made to the D^2 law droplet combustion theory. Beckstead concluded the D^2 as in Equation 2.15 was applicable to larger particles (>20μm). This is of importance to this effort in which 16 - 32 μm sized particles were used.

$$t = \frac{D_0^2}{\beta} \tag{2.15}$$

D_o (μm) is the original diameter of the aluminum particle, t (ms) is the amount of time an aluminum particle was burning after ignition. Equation 2.16 provides the value of β in terms of the radius (r), height (h).

$$\beta = \frac{4\pi r}{\pi D} \tag{2.16}$$

Equation. 2.17 was developed by Belyaev, et al. [1968] to analyze burn rates of aluminum incorporated into propellants to avoid agglomeration:

$$\tau = 0.67 \frac{D^{1.5}}{a_k^{0.9}} \qquad (2.17)$$

with a_k as the relative concentration of CO_2 and H_2O in the gas, and τ as the burning time (ms). Also, they were able to observe the ignition time of such particles and determined that it was proportional to D^2 although the exponential may vary [Beylaev, 1968].

In efforts to decrease the ignition temperature, coating aluminum particles with a metallic material has been considered. Studies about the efficiency of ignition and the burning of aluminum have increased in recent years. Kumar, Fitz-Gerald and Singh [1998] were able to successfully coat spherical alumina particles with yttrium barium copper oxide (YBCO) and praseodyminum barium calcium manganese oxide (PBCMO) within a chamber between 200 and 300 mTorr of oxygen partial pressure.

Hahma, Gany and Palovuori [2006] conducted an experiment using nickel and cobalt as coating elements. Coating the particles intensified the ignition of the samples and accelerated the burn rate in the presence of air but promoted a strong agglomeration of aluminum oxide [Hahma et al., 2006]. An inter-metallic reaction between the aluminum and the metal coating aids the ignition of the aluminum particle by providing a heat pulse. The coating was applied using an electro-less nickel or cobalt plate solution on spherical aluminum powder.

2.3.2 Hencken Post-Flame Burner

Experiments conducted thus far on aluminum particle combustion have utilized a shock tube or burner/laser to ignite single particles. Ellis [2010] conducted ignition and

burn time experiments using a post-flame burner. Particle samples he coated using the PLD system placed in a glass tube called a fluidized bed feeder. The beads of diameters 3nm and 100μm helped to reduce agglomeration of the particles.   A conical diffuser and a conical nozzle were located at the ends of the cylindrical feeder. A 400 mesh sieve with 45 μm openings was placed on top of the conical nozzle to further reduce large agglomerates from entering the post-flame zone.

A honeycomb matrix of stainless steel tubes formed the top surface of the burner. A schematic of the multi-diffusion burner system is shown in Figure 2.6. This uniform post-flame region merged to form a 38 nm diameter flat flame. The post flame region led to a flat flame that ignited and burned the particles as they escaped the surface. Argon and oxygen gas filled tubes around the flat flame. The bordering tubes flowed nitrogen to prevent atmospheric oxidizers from interfering with the ignition and combustion process. A control panel was used to adjust the gas ratio applied to the flame.

The particle burn times were collected using a photo-multiplier tube connected to a data acquisition system (InstruNet model 100B). The system used the data to form charts in MatLab or Tec Plot 360 2008 of time versus intensity [Houim, Boyd and Kuo, 2008]. The particle ignition temperatures were calculated after sufficient combustion data was gathered.
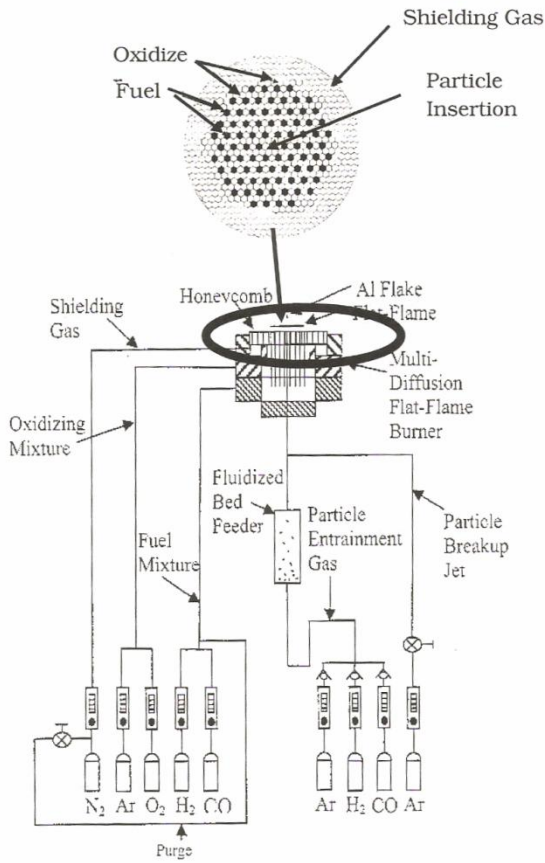
Figure 2.6 Hencken Post-flame combustion flow schematic [Houim et al., 2008]

Experiments conducted on Ni-coated aluminum particles in a post-flame zone of a multi-diffusion flat-flame burner showed a reduction of ignition temperature for 32 μm particles to 1100 K [Boyd et al., 2009]. The effective mole fraction and measured ignition temperatures are presented in Equation 2.17 and Figure 2.7, respectively.

$$X_{OX,eff} = X_{O_2} + 0.5X_{H_2O} + 0.22X_{CO_2} \qquad (2.17)$$
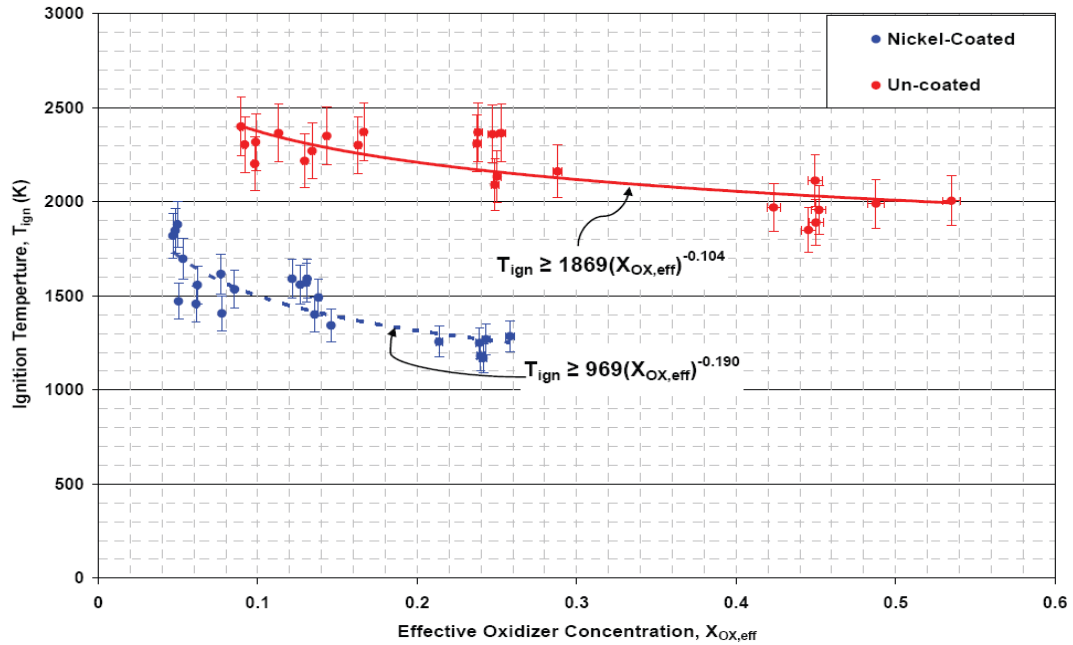
Figure 2.7 Ignition temperatures of 32 µm aluminum particles [Boyd et al., 2009]

2.3.3 Ballistic Compressor

The detonation conditions of a thermobaric weapon consist of high pressures and extreme heating rates which were not attainable in current testing apparatuses. The current techniques have provided useful information on reactive aluminum particles but experiments were conducted in relatively low pressures (< 30 atm) and heating rates much lower than the conditions of TBX. The use of experimental ballistic compressor facility has been proposed to study the ignition and combustion of energetic fuel particles in conditions reminiscent of TBX detonation [Kuo, 2010]. Prior studies utilizing a ballistic compressor evaluated the erosive effects of high temperature and pressure gas on metals and liquid propellant jet propulsion [Birk and Kooker, 1998].

28

The ballistic compressor was broken into four components labeled in Figure 2.8. The entire length of the device was 6.78 meters (22.28 ft) including the compression tube of 3.96 meters in length [Sirignano, 2011]. Further details of the Ballistic Compressor dimensions are provided in Appendix A. Removal of the test section allowed access to load the piston and particle sample between each firing. The piston was pushed upstream towards the gas reservoir using a ram rod. The test section was replaced and instrumentation devices connected. After the desired amount of gas pressure was achieved in the reservoir, the test was initiated and data was recorded from the ignition event that transpired in the test section. At the conclusion of the test, the pressure release values were opened to empty the gas reservoir and flow atmospheric air into the compression tube. Hearing and eye protection was used during preparation, testing and post testing disassembly of the device. Additionally, an enclosure was constructed to military specifications consisting of ¼" steel plates to enclose the test section and transition section in the event of a catastrophic failure.

Figure 2.8 120 kpsi ballistic compressor at PSU [Sirignano, 2011]

The device utilized a driver reservoir of gas to move an inertial piston, rapidly compressing the gas in the tube into the test section with the sample of aluminum particles. The schematic of this process is shown in Figure 2.9. Ideally, the particles would absorb enough heat to ignite. The system has the capability to reach temperatures up to 10,000K and pressures in excess of 100 kpsi [Kuo, 2010]. Prior to experiments conducted at the PSU High Pressure Combustion Lab, ballistic compressors had not been used to study TBX weapons.
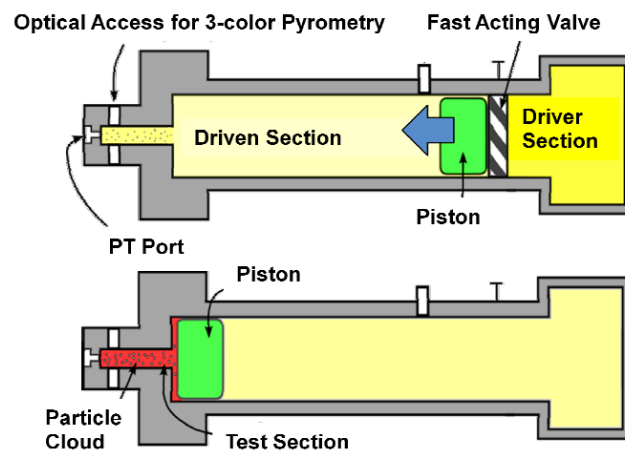
Figure 2.9 Ballistic compressor operation before and after firing [Kuo et al., 2010]

Sirignano [2011] was able to successfully modify a ballistic compressor to capture a combustion event in a controlled process. He utilized a Hamamatsu H8249-102 three-color pyrometer (PMT) to capture light emitted from the reactive particles which can be used to calculate temperatures [Sirignano, 2011]. However, due to the experimental nature of the apparatus, combustion temperatures were not attainable using

the PMT since the neutral density filters were over saturated, indicated in Figure 2.10 by

the plateaus.
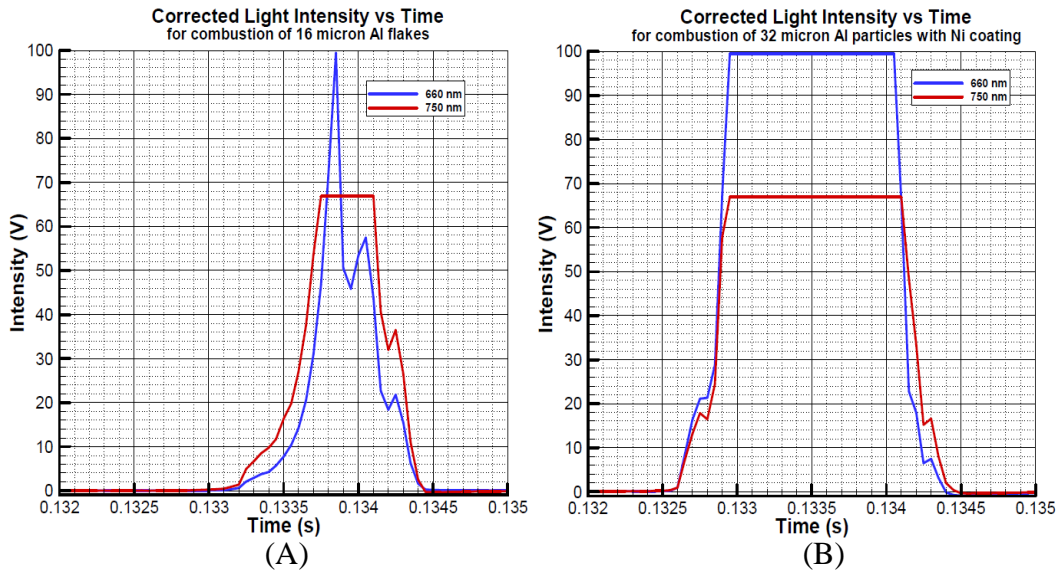
**Figure 2.10 Light intensity-time traces of 660 and 750 nm wavelength emissions
using (A) SilberCote Al flakes, (B) Technion 32 μm Al particles
coated with Ni [Sirignano, 2011]**

Several tests were completed with the ballistic compressor to validate the test

section modification made by Sirignano. The actual data collected from the PMTs,

pressure transducers and thermocouples was compared to a prediction model made using

MATLAB software. The actual data fell within the predicted range with a degree of

error, but Sirignano concluded that more testing of the device should be completed once

further mechanical modifications had been made.

CHAPTER 3

EXPERIMENTAL PROCEDURES AND MATERIALS

This chapter provides details of the process and materials used to coat the aluminum particles. The alternative modifications considered to further enhance the coating of the particles are discussed. Lastly, this chapter provides an overview of the characterization methods chosen.

3.1   Modifications to Pulsed Laser Deposition System

The device used to coat the aluminum particles in previous experiments was a Pulsed Laser Deposition System (PLD). The original configuration of the PLD target-substrate interaction was previously shown in Figure 2.1. Generally used for coating solid, flat surfaces, several possible configurations were considered by Ellis to develop a method to coat two-dimensional aluminum flakes. These options included: using double sided tape to attach particles to the substrate holder, reorienting the laser box, using a series of reflectors to redirect the laser beam, and redirecting the target plume.

Due to the nature of the size of the laser box, moving this object was not a feasible solution. Use of the reflectors would necessitate the need to mount the reflectors inside the deposition chamber, which was undesirable. The difficulty of adjusting the alignment of the laser beam would have also been an issue for this configuration. Lastly, utilization of the double sided tape would only allow one side of the two-dimensional flake to be coated and extreme chamber contamination would occur which was also

undesirable. A schematic of the logical configuration chosen by Ellis is seen in Figure 3.1.
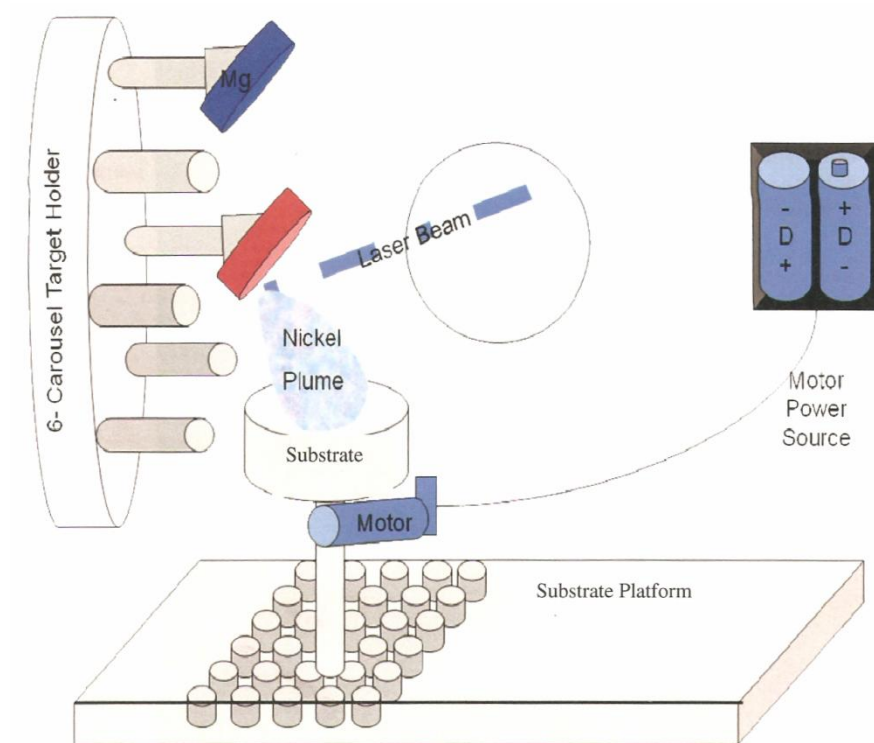
Figure 3.1 Aluminum Particle Coating Configuration [Ellis, 2010]

To decrease the risk of contaminating the PLD chamber, the aluminum particles were placed in a horizontally oriented container. A 19-x-3.5 inch platform was used to span the diameter of the chamber and support the particle holder in position below the target. The base of the particle holder was fitted with threads to allow for adjustability of the height and position in relation to the target. To accomplish redirecting the target plume, a 45-degree angle was machined on the stem of a target holder. The two pieces

created were welded back together with the holder facing downward towards the particle holder. Figure 3.2 is a photo of the angled target and particle holder platform inside the deposition chamber.
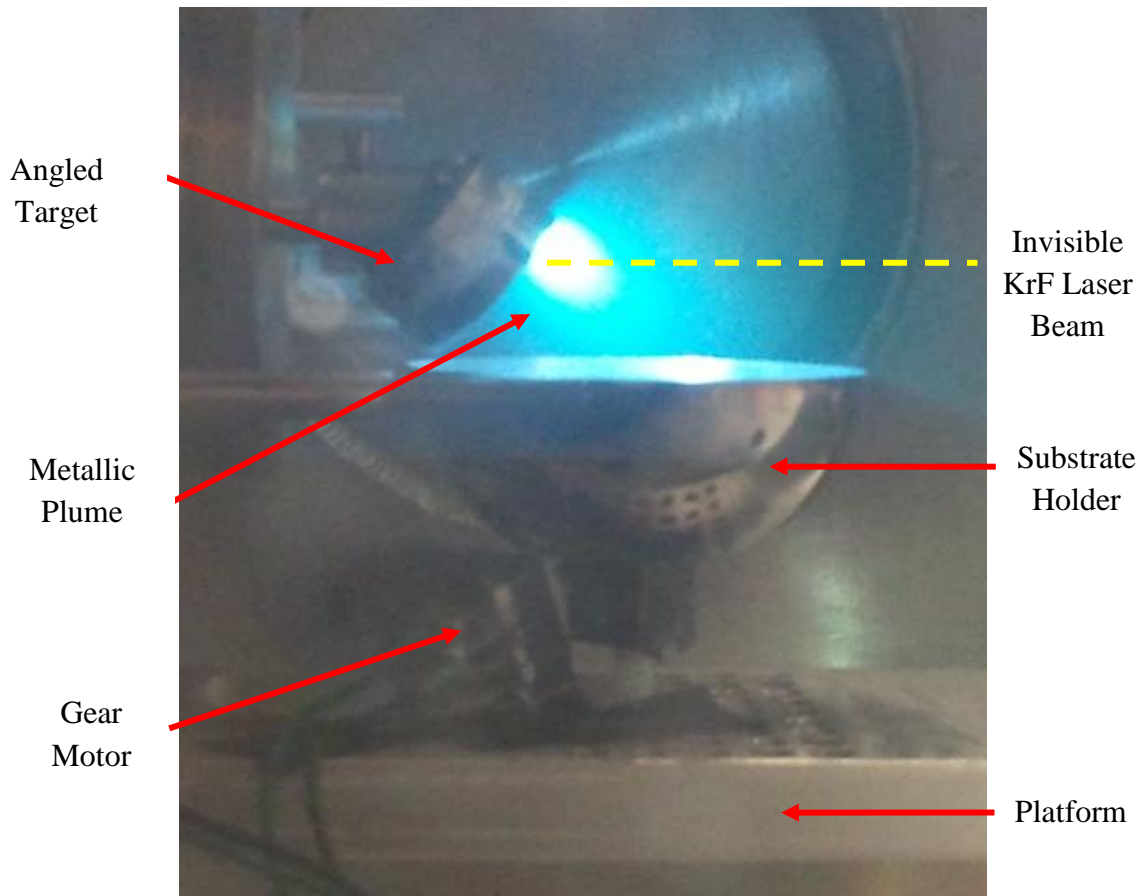
Figure 3.2 Particle holder platform inside chamber

It was desired to create agitation of the particles to increase the likelihood of exposure to the target plume. Vibrating the base of the particle holder with a geared motor introduced a mixing effect which promoted particles at the bottom of the substrate holder to surface. A thin piece of aluminum measuring 1 x 3/8 inch was attached to the

gear shaft creating centric loading and more vibration of the particles. To power the motor, two 1.5V D batteries were used as the power source. The power source was located outside of the chamber to avoid potential leakage of the battery acid caused by the vacuum system. The PLD system was equipped with an eight-pin electrical feed-through that allowed power transmission into the chamber as see in Figure 3.3.

| (A) | (B) |

Figure 3.3 (A) Electrical pin feed-through outside chamber, (B) Feed-through inside chamber

The modifications to the PLD system by Ellis allowed for coating of the particles, but the configuration had several flaws. By angling the target holder, the 360 degree rotation feature of the system could not be utilized without redirecting the target plume away from the aluminum particles. Instead the target was rastered with a 10-degree range to prevent damage of the target from a concentrated laser pulse. Additionally, the substrate holder of the original chamber design was equipped with a heater to improve the effectiveness of the deposition process. Moving the particles holder to a horizontal

position negated the use of this feature. Efforts were made to monitor the amplitude of the vibration but particles some were spilt during the deposition of the two gram samples which was undesirable. For these reasons, it was apparent to consider further modifications to the PLD system. The options explored are listed in Table 3.1 with their respective advantages and disadvantages.

Table 3.1 Potential Modifications to PLD System

Modification	Pros	Cons
Increase vibration of the particle holder	Better particle coating Current apparatus setup used	Spillage of particles, contaminating testing chamber
Change size/geometry of particle holder	No modification to procedures Less contamination of chamber	Particles may neglected from target plume if holder is too deep
Incorporate a rotating arm inside particle holder	Better particle coating	Machine or purchase device May require additional power source
Add glass beads to agitate the particles	Better particle coating Current apparatus setup used	Particles may cling to beads
Position target and particle holders closer than 2.5 inches	Better particle coating	Limited clearance between holders
Use spherical particles	No modification to procedures Easier to coat particles Collaboration on other research	Increased material cost

The feasibility of each modification was taken into consideration and ultimately the use of spherical particles and changing the size and/or geometry of the particle holder were selected as the appropriate modifications for this research. Three particle holders were selected to test with particles independent of the testing chamber as seen in Figure

3.4. The degree of particle agitation was noted using increments of 0.1, 0.3, and 0.5 grams of aluminum spheres as sample sizes. Holder (A) created the best vibration of the sample mass. The tests conducted with Holder (B) had similar results to Holder (A) as expected due to the likeness in geometry. The base of holder (C) was thicker than (A) and (B) which may have dampened the vibration of the particles. The data gathered from testing the various particle holders is presented in Appendix B. Holder (B) was ultimately chosen over (A) due to the shallower depth providing optimal exposure of the target plume to the aluminum particles.
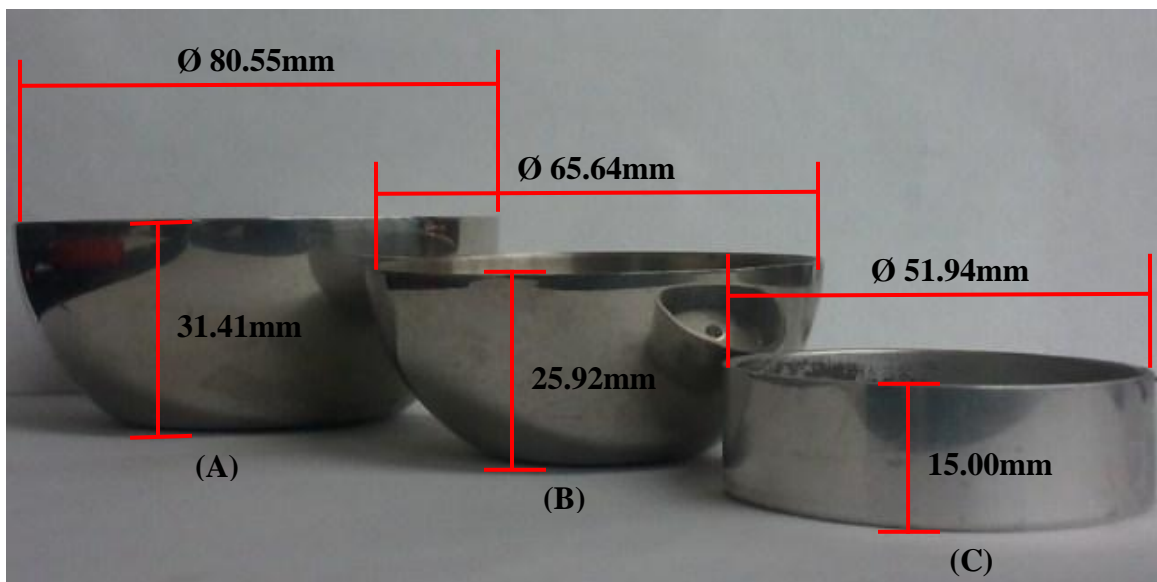
Figure 3.4 Particle Holders

3.2   Target and Sample Preparation

The process of the laser ablating the target creates a unique pattern during depositions. To prevent damage to the target from repetitive depositions, sandpaper is

used to polish the target surface creating a smooth surface. The top of the target holder is also sanded to remove remnants of silver paste from previous depositions. The smooth target is then mounted onto target holder using silver paste and placed on a heater to dry. Once dry, the target holder was positioned and tightened onto the target carousel holder pointing downward towards the aluminum particles.

The desired sample size of aluminum particles and measured by first placing a small, measuring container onto the mass scale and using the zeroing function to neglect this mass. Aluminum flakes or spheres were added to the container until the desired mass was reached. The mass was noted and the aluminum particles were carefully poured into the particle holder.

3.3   Chamber Preparation

To prepare for each deposition, gloves were worn to clean the PLD chamber and its components with acetone preventing contamination from oils and particles. The particle holder, platform, gear motor and platform were cleaned with isopropyl. Next, the laser box was switched into the "ON" position to allow time for the laser to warm up while other tasks were completed. The electrical feed-through seen in Figure 3.3 was removed to attach and secure the wires for the motor and power source making sure to align the pins. Following this step, the power supply to the motor was checked after the electric feed-through was replaced. The platform and target were placed inside the chamber and laser beam pulses were released to check their positioning. Rotation of the target was not applicable for these experiments therefore, the command was turned off.

Additionally, the motor to raster the target was started to insure there was no interference with the particle holder.

After final adjustments were completed, the pressure release valve and chamber openings were closed in preparation for vacuum. The vacuum pump was turned on and depressurized the chamber to 3.0 x 10^{-5} Torr atmosphere. This process took approximately 75 minutes. During this time, the laser's commands for pulse and dispersion rate were set. At the conclusion of the deposition, the gear motor power source and target raster was turned off. The pressure release valve was opened and while the vacuum pump was turned off. Lastly, the platform was removed to extract the particles and the chamber was wiped down and closed until needed for further depositions.

3.4 Experimental Design

In these experiments, magnesium and nickel are used to coat aluminum spherical particles and aluminum flakes. The equipment and laser specifications set by Ellis were replicated. An 18 inch Neocera PLD system was used for the depositions. The excimer Krypton Fluoride (KrF) laser with wavelength 248 nm and pulse duration was set to 20 ns was to ablate the targets. The laser energy was reduced from 700 mJ to 600 mJ. The pulse rate and energy density were maintained at 25 Hz and approximately 1 J/cm^2, respectively.

Ellis used a particle holder similar to holder (c) with a depth of 15mm. The depth of Holder (b) selected for these experiments was greater than the depth of holders previously used. This created interference with the target raster. The orientation of the

motor was changed from vertical to horizontal to increase the amount of space between the motor and platform. The threads on the motor and particle holder assembly were utilized to lower the top edge of the particle holder. Ellis' target-to-substrate distance was held at 2.5 inches [Ellis, 2010]. The target-to-substrate distance in this experiment was reduced to 2.0 inches. A substrate holder mount that had not yet been fitted with a heater was used to close the chamber opening in place of the convention substrate heater that was not used.

The mass of the particles was approximately 500 mg. The main variable that differed for the experiments was the coating element, Ni vs. Mg. The geometry of the aluminum particles was varied. The pulse frequency was held consistent with the first experiments of Ellis at 20 pulses per second for 30k pulses. The experiment took approximately 25 minutes. In the second experiment, the mass and laser parameters were unaltered. This experiment was conducted to examine the increases of deposited target material due to increased plume exposure.

A mechanical failure of the gear motor was experienced 12 minutes into one of the depositions, leaving only the top portion of particles exposed to the target plume. The excessive vibration of the motor caused the platform to shift, moving the particle holder away from the plume and exposing the motor to the intense heat of the laser. As a result the motor mount was fused to the motor, seen in Figure 3.5. The deposition was completed since the failure presented no harm to the functionality of the laser and chamber. The container containing the particle sample from that deposition was labeled and set aside for review using SEM.

(A)   (B)
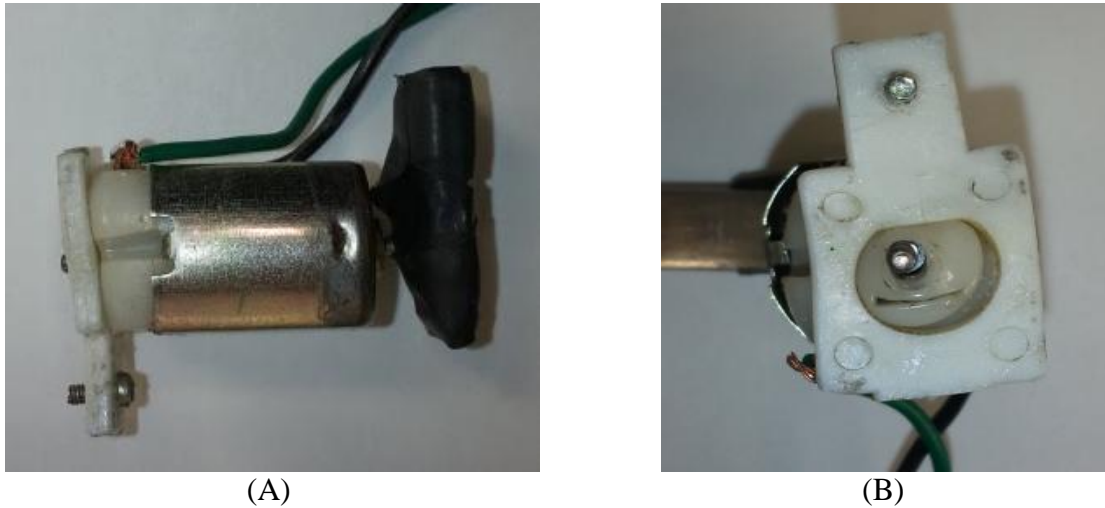
Figure 3.5 Deformation of motor due to laser heat exposure (A) side view and (B) front view

3.5   Hencken Burner Characteristics

Burn time data was analyzed during this reporting period. Ellis [2010] collected data at The Pennsylvania State University during his research on Controlled-Coating of Aluminum Nano-Particles for Ignition and Combustion Studies. Table 3.2 shows the burn time data for uncoated and coated flakes, burning environment H_2/CO and H_2 and an experimental parameter of $\varphi = 0.3$ and $\varphi = 0.4$.

He utilized a qualitative approach to compare the burn times (milliseconds) of each experiment. From graphs, he observed that there were consistencies in the burn times of the uncoated particles but the results of the burn times for coated particles were random [Ellis, 2010].

Table 3.2 Burn Time Raw Data

Coating	Coated	Coated	Coated	Coated	Uncoated	Uncoated	Uncoated	Uncoated
Environment	H2 & CO	H2 & CO	H2	H2	H2 & CO	H2 & CO	H2	H2
Phi Value	0.3	0.4	0.3	0.4	0.3	0.4	0.3	0.4
Letter Assignment	A	B	C	D	E	F	G	H
	1.4	1.5	0.7	3.8	0.7	2.0	0.7	0.8
	1.4	1.1	0.6	3.5	1.5	1.8	0.4	0.7
	0.6	1.3	5.5	3.4	1.2	1.4	0.6	0.8
	1.3	1.2	0.7	6.2	1.2	1.8	0.5	1.0
	2.0	1.6	0.7	3.2	1.8	1.8	0.6	0.7
	1.5	1.4	0.4	3.5	1.4	2.2	0.7	0.6
	1.0	1.4	0.6	4.2	1.4	2.0	0.7	0.7
	1.4	1.1	0.8	0.4	1.2	2.0	0.7	0.7
	0.8	1.0	0.8	0.7	1.0	2.0	0.5	0.7
	0.8	1.1	0.8	2.9	0.8	2.0	0.7	0.7
	1.4	1.0	0.6	0.7	0.8	1.9	0.7	1.0
	1.3	1.2	1.4	6.0	1.4	2.0	0.8	0.8
	0.7	1.2	0.8	7.0	1.4	2.0	1.2	0.6
	0.6	1.5	1.0	1.6	1.7	2.0	1.4	0.7
	0.6	1.2	0.7	3.5	1.25	1.8	0.9	0.7
Average	1.116667	1.25	1.067333	3.365	1.25	1.913333	0.74	0.746667
S.D.	0.42159	0.184197	1.235663	1.985434	0.320156	0.180739	0.261315	0.118723

The data set of numbers in each column represents the burn time in milliseconds for individual aluminum particles that were used for the combustion studies. Once enough data was collected, the average burn time for each batch was calculated along with the standard deviation. These figures would be used for statistical analysis to determine which variation of particle coating, phi value and environment had a significant impact on the burn time of the Al-particles.

CHAPTER 4

RESULTS AND DISCUSSION

Chapter 4 discusses the results and observations from the aluminum particle coating experiments. The burn time data obtained from Ellis factored in the burning environment and phi value. Statistical analysis is used to analyze the results.

4.1   Aluminum Particle Burn Time Data

Ellis employed graphical analysis to examine any consistencies in the burn times of the uncoated and coated aluminum particles. His analysis was inconclusive and the data did not support the theorized conclusion. Thus, it was desirable to perform a quantitative comparison between the burn times of coated versus uncoated aluminum flakes.

Based on the sample size of 15 burn times (particles), a statistical test was used to find the 95 percent confidence limits of the burn time for each particle. The limits were calculated and presented in Table 4.1. Theoretically, by comparing the confidence limits of two conditions, statistical conclusions could be drawn pertaining to whether or not particular particle conditions or burning environment would have a significant effect on the burn time. The factors that show significance would then be further investigated for a better understanding of the desirable coating characteristics and to develop methods to achieve these characteristics.

Table 4.1 Burn time comparison: 95% confidence limit

	Condition 1 vs. Condition 2	Limits: Condition 1		Limits: Condition 2		Comments
Coating	H_2/CO with φ=0.3 Coated (A) vs. Uncoated (E)	0.883	1.350	1.0727	1.4273	Overlap, No significant difference
	H_2/CO with φ=0.4 Coated (B) vs. Uncoated (F)	1.1480	1.3520	1.8132	2.0134	No overlap, Significant difference
	H_2 with φ=0.3 Coated (C) vs. Uncoated (G)	0.383	1.752	0.5953	0.8847	Overlap, No significant difference
	H_2 with φ=0.4 Coated (D) vs. Uncoated (H)	2.226	4.464	0.6809	0.8124	No overlap, Significant difference
Environment	Coated, φ=0.3 H_2/CO(A) vs. H_2(C)	0.883	1.350	0.383	1.752	Overlap, No significant difference
	Coated, φ=0.4 H_2/CO(B) vs. H_2(D)	1.1480	1.3520	2.226	4.464	No overlap, Significant difference
	Uncoated, φ=0.3 H_2/CO(E) vs. H_2(G)	1.0727	1.4273	0.5953	0.8847	No overlap, Significant difference
	Uncoated, φ=0.4 H_2/CO(F) vs. H_2(H)	1.8132	2.0134	0.6809	0.8124	No overlap, Significant difference
Phi Control	Coated, H_2/CO Φ = 0.3 (A) vs. Φ=0.4(B)	0.883	1.350	1.1480	1.3520	Overlap, No significant difference
	Coated, H_2 Φ = 0.3 (C) vs. Φ=0.4(D)	0.383	1.752	2.226	4.464	No overlap, Significant difference
	Uncoated, H_2/CO Φ = 0.3 (E) vs. Φ=0.4(F)	1.0727	1.4273	1.8132	2.0134	No overlap, Significant difference
	Uncoated, H_2 Φ = 0.3 (G) vs. Φ=0.4(H)	0.5953	0.8847	0.6809	0.8124	Overlap, No significant difference

The following conclusions were drawn regarding magnesium coated aluminum flakes. The coating increased the average burn time from 1.25 ms to 1.91 ms for an H_2/CO environment and $\varphi=0.4$ but no significant difference for the same environment with $\varphi=0.3$. The coating increased the average burn time from 0.747 ms to 3.365 ms for a H_2 environment and $\varphi=0.4$ but no significant difference for the same environment with $\varphi=0.3$. For coated flakes, the H_2 environment increases the average burn time from 1.25 ms to 3.365 ms over H_2/CO environment for a $\varphi=0.4$, but no significant difference was observed for the same environment with $\varphi=0.3$. Similarly, the uncoated flakes in a H_2/CO environment increased the average burn time for the H_2 environment for both values of φ but the improvement is very small, though statistically significant.

4.2   SEM Characterization

Visual Characterization of the coated and uncoated aluminum particles was performed with the Scanning Electron Microscopy (SEM). The SEM is a nondestructive analysis method to produce high-resolution images of a sample surface under a range of 20X to upwards of 25,000X magnification. The SEM allows adjustments to the magnification, contrast, brightness and focus of the image that is desirable in these experiments. This is an accurate way to visually examine the surface structures of the sample. The SEM module used was also equipped with Energy Dispersive X-Ray Spectroscopy (EDS) system providing the capability to perform elemental analysis of the specimen. A detector in the SEM converts the X-ray energy into voltage signals used to determine the unique characteristics of each element's atomic structure [Swapp, 2007].

Double-sided tape was used to mount particles from each sample on the stage for SEM imaging. The resulting images from a sample of the aluminum flakes characterized are represented in Figure 4.1. The yellow, dashed lines highlight an area in each image that was selected for viewing under higher magnification to better assess the surface characteristics. The images were evaluated on the precedence that coated aluminum particles would appear brighter than the uncoated Al particles due to a variance in conductive materials exposed to the electrons from the microscope.
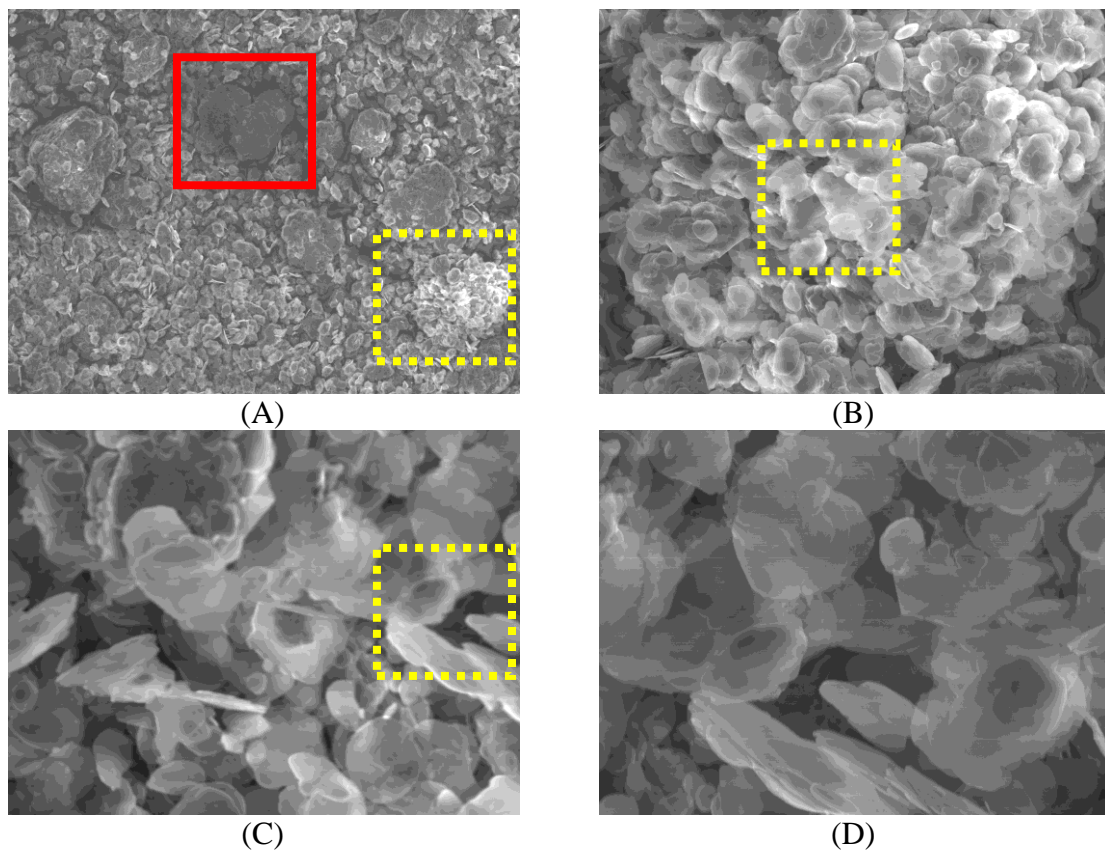

(A)

(B)

(C)

(D)

**Figure 4.1 SEM images of a sample of Al flakes-Ni at multiple magnifications
(A) x450, (B) x900, (C) x1500, and (D) x2000**

The aluminum particles are more conductive and attract fewer electrons from the microscope to its surface dimming the responsive light. The sample in Figure 4.1 (A) displays the inconsistencies of the applied coating. Additionally, the larger clusters may be a result of agglomeration. During handling of the particles before and after deposition, a magnetic charge was experienced between the Al-particles and tools used for manipulation.

Figure 4.1 (A) was taken under the least amount of magnification and represents an overall view of the particle sample. Based on the methodology for determining the particles that were coated, majority of the particles in the sample received some amount of deposited metallic material. However, there is a large cluster of particles outlined in a red box that displays dim contrast indicating those particles were not exposed to the target plume. Figure 4.1 (B) is a magnified image of the brightest particle cluster from Figure 4.1 (A). All of the particles in this image are of brighter contrast indicating they were successfully coated with a thin-film of Nickel. More of the surface details can be seen in Figure 4.1 (C) and (D) along with the side profile of the flake. Additionally, it is apparent that some of the Al-flakes were only coated on the outer edges. This occurrence may be a result of the constant movement of the flakes due to the vibration of the holder during the deposition process. The red box in Figure 4.1 (D) highlights a flake with illuminated edges while the center portion is of dimmer contrast.
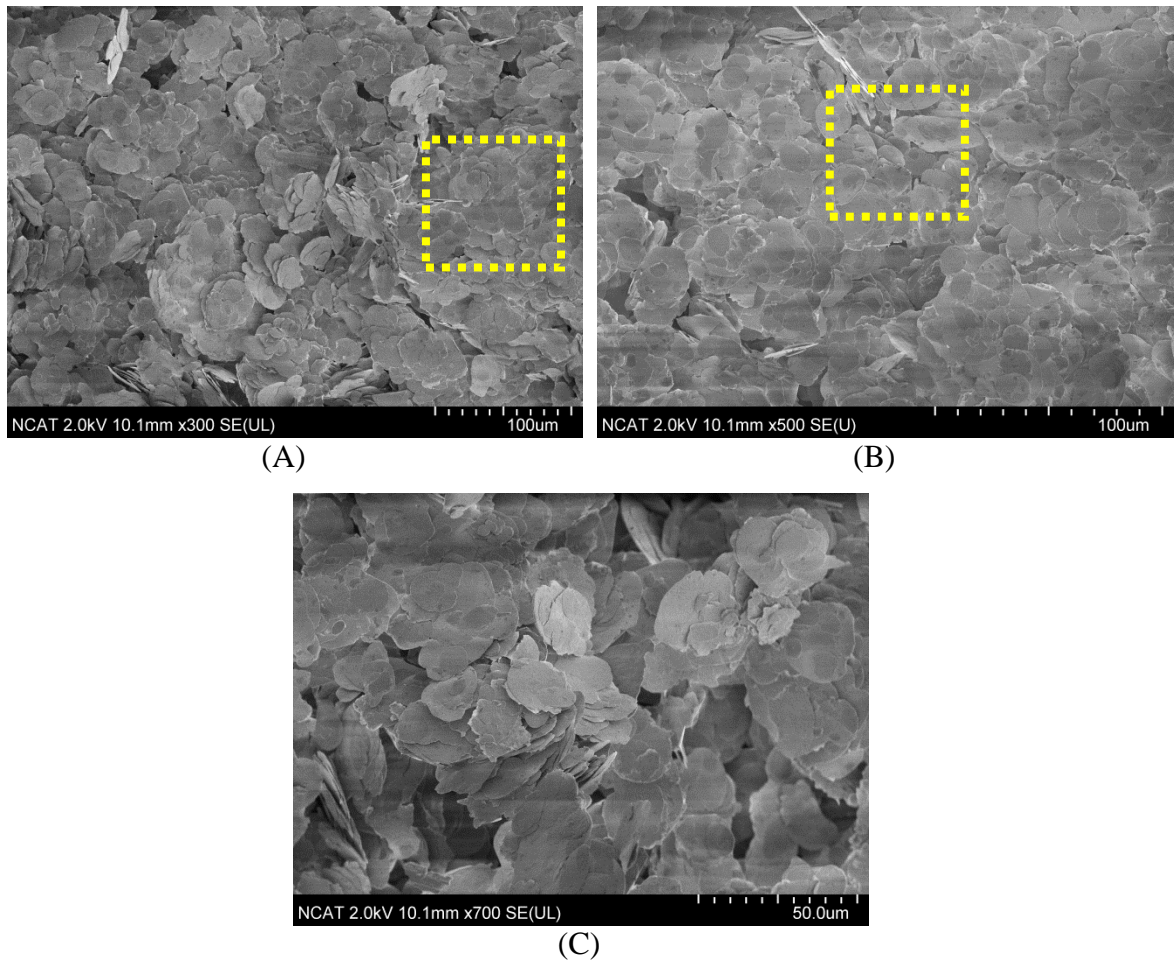
Figure 4.2 SEM images of sample of Al flakes-Mg at multiple magnifications (A) x300, (B) x500, and (C) x700

Majority of the Al-flakes in the sample used for imaging were coated with Mg along their edges. These images were captured under a different contrast and brightness setting, thus the brilliance reflected by the Mg-coating is not as easily identifiable. Figure 4.2 (A) was taken under the least amount of magnification. In Figure 4.2 (B), the outlines of several darker droplets appear on the surface of the flakes which can be identified as Mg. The outlines give the viewer a better representation of the inconsistency of the

deposition method used in this research which is also confirmed under the higher magnification if Figure 4.2 (C). The contrast and brightness were adjusted before the sample was imaged for Figure 4.3.
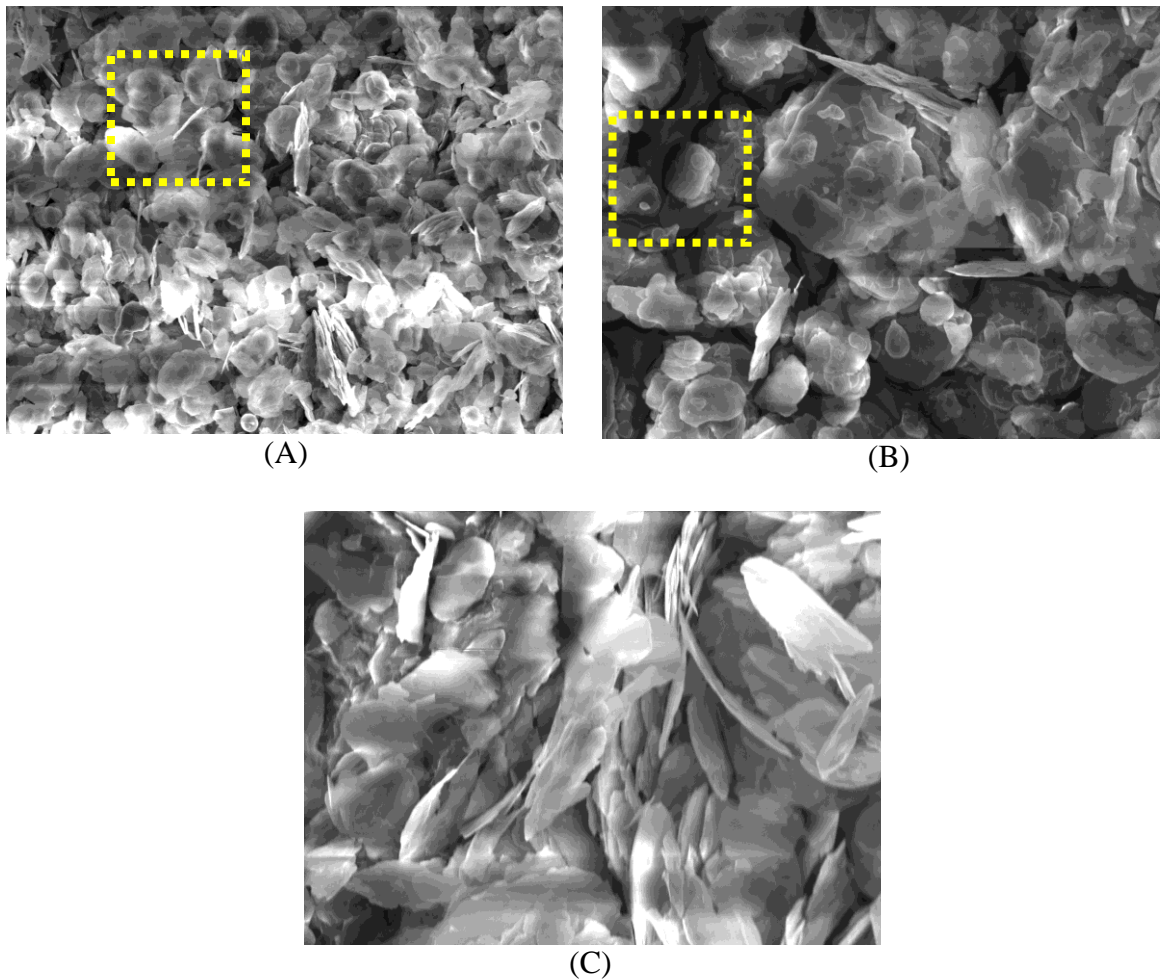

Figure 4.3 SEM images of sample of Al flakes-Mg at multiple magnifications (A) x450, (B) x900, and (C) x1500

Figure 4.3 (A) was taken with a 450X magnification. There are three apparent horizontal lines of brightly illuminated Al-flakes; however, the significance of this

pattern is unknown. Figure 4.3 (A) is a good representation in the contrast between particles that received the most exposure to the target plume and those that did not receive any deposit Magnesium. The magnified area from Figure 4.3 (A) is captured in Figure 4.3 (B). Again, there are outlines of Mg-droplets visible on the surface of the flakes. The edges of these droplets appear brighter in the image compared to those identified in Figure 4.2 (B). The difference in brightness may be attributed to the changes in brightness and contrast settings. Although, some of the Al-particles seen in The highlighted area of Figure 4.3 (B) was magnified to 1500X. More of the surface details can be seen in Figure 4.3 (C). At the higher magnification, it is evident that this section of particles was exposed to the target plume and majority of the particles were coated with the exception of those deeper into the sample being viewed.

Figure 4.4 (A) is the least magnified representation of another Al-flakes batch coated with Nickel. Approximately 50% of the sample is coated. The 900X magnified area seen in Figure 4.4 (B) has similar characteristics as previous samples with deposited material being identified along the edges of the flakes. Figure 4.4 (C) shows the outlines of darker droplets appearing on the surface of the flake. At the higher magnification, the deposition consistency level is still approximately 50%.

(A)   (B)

(C)
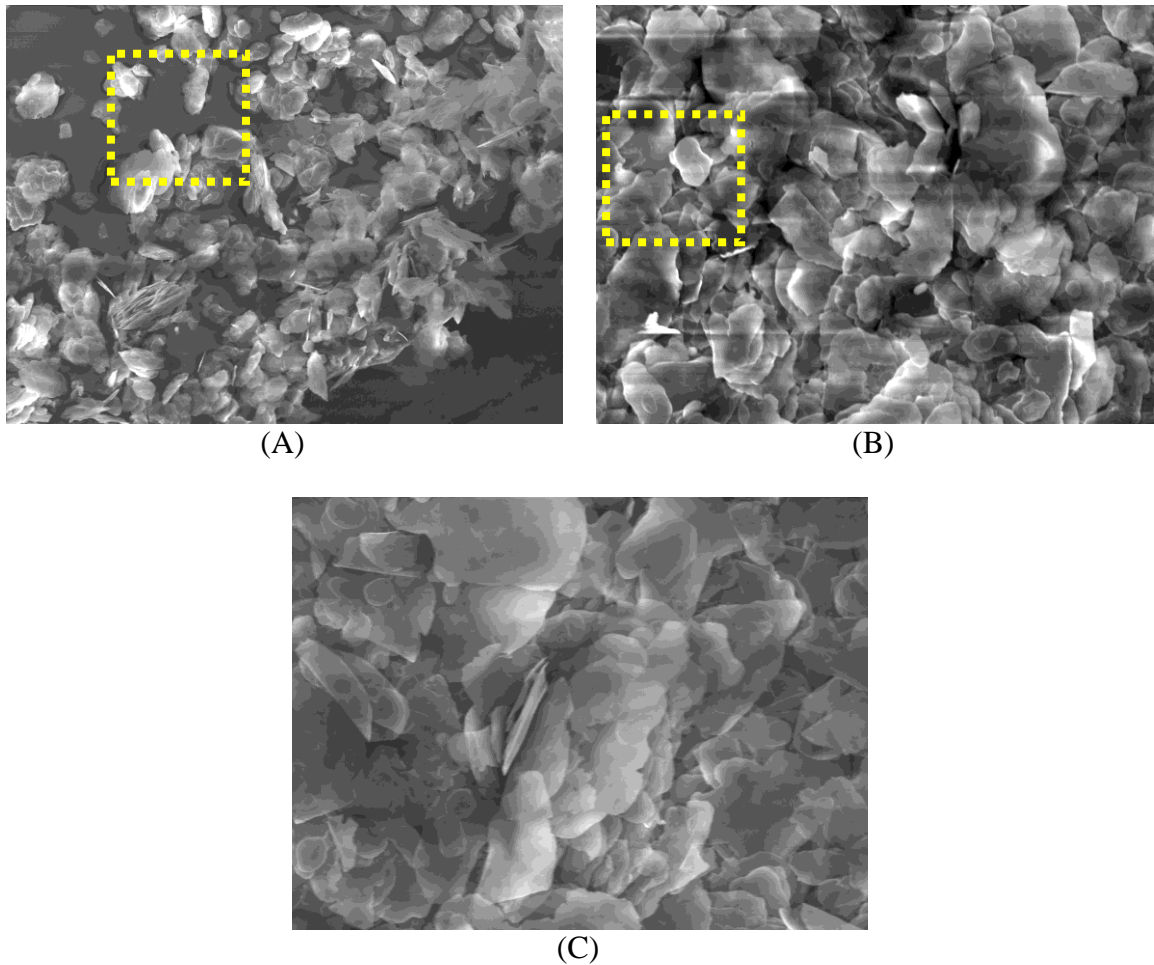
Figure 4.4 SEM images of sample of Al flakes-Ni at multiple magnifications
(A) x450, (B) x900, and (C) x1500

In the second experiment, the samples were exposed to the target plume for an extended amount of time in efforts to increase the amount of deposited material. The dimness of Figure 4.5 (A) indicates a very minimal coating of the aluminum flake surface. There are clusters of particles with a trace amount of reflective material represented in the figure. The particle sample used for SEM could have been on the bottom of the particle container and received less exposure to the deposition plume. Figure 4.5 (B) is marginally brighter, with a greater number of particles coated by the

magnesium. The images are also affected by the visual characteristics of the operator that has the ability to control the focus, contrast, brightness of the image displayed.

(A)   (B)
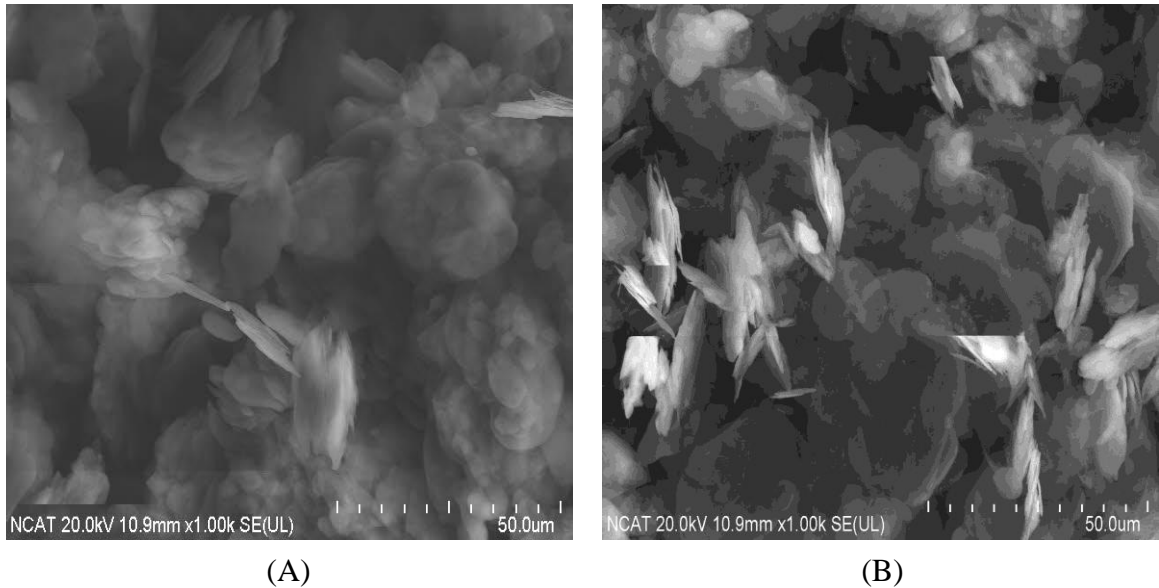
**Figure 4.5 SEM images of Mg coated Al flakes (A) after one deposition
(B) After two depositions**

As a result the images in Figure 4.2 indicate minimal traces of the coating material. Additionally, the contrast and brightness of these images is very low. The motor was replaced before the next deposition. The sample chosen for Figure 4.3 represented the best deposition. Majority of the particles received a coating of magnesium as indicated by the brightness of the image. Many of the particles received even coatings, unlike the previous samples which is evident at higher magnifications. The last SEM sample, also had positive results. A range in particle sizes was observed but several particles were evenly coated, while others were only coated on the edges.

CHAPTER 5

CONCLUSIONS

The goal of this research was to modify a pre-existing experimental deposition method to enhance the surface and combustion properties of aluminum particles. The effects of the process on the surface morphology of the coated particles and their effect on the ignition properties were studied using SEM and EDS. The inability of the initial technique to produce a uniform coating on Aluminum particles with Magnesium and Nickel was to be corrected.

Vibrating the particle holder during the deposition was beneficial for agitating the particles and exposing them to the target plume. The use of vibration was also deemed necessary due to an increase in the size of the particles compared to those used in previous experiments. Three particle holders of varying sizes were tested with particles independent of the testing chamber and the degree of particle agitation was noted. The holder with the median volume was ultimately chosen to accommodate the larger particles while still providing optimal exposure of the target plume to the aluminum particles. During testing, the Teflon coating on the aluminum flakes was observed to encourage the unwanted adhesion of the particles to the sides of the holder. As a result, the particles were either exposed only to the Mg plume on one side of the flake or not exposed to the plume at all.

The geometry of the particles presented several issues during visual characterization with the Scanning Electron Microscopy. It was very difficult to obtain

images of the aluminum without encountering particles in the vertical position. The contrasting areas of brightness were perceived to indicate the difference in the coated and uncoated areas. Based on this methodology of identifying the coated particles, it was evident some of the samples used for imaging had minimal traces of the coating material. The two samples exhibiting the best uniform coatings were coated with Magnesium. During visual characterization of the Al-particle surface, some of the particles were displayed brighter illuminations along their edges which may have been a result of the vibration system.

In future experiments, several modifications and adjustments could be made to the PLD coating process. Some of these adjustments include replacing the battery powered gear motor and machining sturdier gear mounting pieces. Additionally, attaining samples from different depths of the particle mass would be beneficial to indicate if the particle coating varied based on exposure to the target plume. Obtaining EDS data for the Ni-coated particles without causing damage to SEM under high voltage is also desired. Lastly, upon further improvements to the ballistic compressor temperature instrumentation, it would be very advantageous to TBX research to compare the particles coated by PLD to those manufactured by Technion and SilberCote.

The results of the modifications to the PLD coating process demonstrated that the process is capable of depositing a thin-layer of the desired metallic element on the Al-flakes. The SEM images also highlighted the uniform film growth inconsistencies. Prolonged exposure to the target via increased number of pulses seemed to have no significant impact on the element composition. Lastly, the method lacks the ability to

produce large masses of particles without sacrificing the cleanliness of the chamber. The

current inability to scale the PLD coating process up to mass production is an important

factor for consideration of the method by weapons manufacturers and military research

agencies. Although technological improvements have been made, the deposition rates of

PLD are presently inferior to those of other thin film deposition methods. Other methods

for coating aluminum particles with a thin metallic layer are to be employed.

REFERENCES

Andor Technology. (2010). *Pulsed laser deposition (PLD) & plasma plume investigations*. Retrieved from http://www.andor.com/learning/applications/Pulsed_Laser_Deposition/.

Babuk, V. A., Vassiliev, V. A., & Sviridov, V. V. (2001). Propellant formulation factors and metal agglomeration in combustion and aluminized solid rocket propellant. *Combustion Science and Technology*, *163*(1), 261-289.

Beckstead, M. W., Newbold, B. R., & Waroquet, C. (2004). *A Summary of aluminum combustion* (Tech. No. N00014-95-1-1338). Multidisciplinary University Research Initiative, Brigham Young University.

Beckstead, M. W. (2005). Correlation aluminum burn times. *Combustion, Explosion, and Shock Waves*, *41*(5), 533-546.

Belyaev, A. F., Frolov, Yu. V. and Korotkov A. I. (1968). Combustion and Ignition of Particles of Finely Dispersed Aluminum. *Combustion, Explosives and Shock Waves*, 4(3), 323-329.

Birk, A., & Kooker, D. E. (1997). *A Ballistic compressor-based setup for the visualization of liquid propellant jet combustion above 100 Mpa.* Department of the Army, Army Research Laboratory. Technical Report.

Boyd, E., Houim, R., Kuo, K. (2009). Experimental and Numerical Investigation into the Ignition and Combustion of Aluminum Particles with TBX Applications, Presented at 1st National Capital Region Energetics Symposium, April 27-28, La Plata, MD, USA.

Child Victims of War. (2010). *Injury mechanism depends on range from detonation.* [Web Photo]. Retrieved from http://childvictimsofwar.org.uk/the-weapons/.

Chourasia, A. R., & Chopra, D. R. (1997). Auger electron spectroscopy. In F. Settle (Ed.), *Handbook of Instrumental Techniques for Analytical Chemistry* (pp. 791-805). Upper Saddle River: Prentice Hall.

Chrisey, D. B., & Hubler, G. K. (1994). *Pulsed laser deposition of thin films*. John Wiley & Sons, Inc.

Claeyssens, F. (2001). *Fundamental studies of pulsed laser ablation*. (University of Bristol).

Defense Threat Reduction Agency. (2008). <htt://www.dtra.mil/>

Dorneanu, L. (2007). *How does a thermobaric bomb work?*. Retrieved from
http://news.softpedia.com/news/How-Does-a-Thermobaric-Bomb-Work-58352.shtml.

Dreizen, E. L., Berman, C.H., and Vicenzi, E.P. (2000). Condensed-phase modifications
in magnesium particle combustion in air. *Scripta Materialia* 122: 30-42. Doi
10:1016/S0010-2180(00)00101-2 (http:/dx.doi.org/10:1016%2FS0010-
2180%2800%2900101-2).

Ellis, M. D. (2010). *Controlled-coating of aluminum nano-particles for ignition and
combustion studies*. (Master's thesis, North Carolina A&T State University).

Escot Bocanegra, P., Chauveau, C., and Gokalp, I. (2006). Experimental studies on the
burning of coated and uncoated micro and nano-sized aluminum particles.

Fournier, V., Marcus, P., and Olefjord, I. (2004). *Oxidation of magnesium*, Department of
Engineering Metals, Chalmers University of Technology, 412-96 Goteborg, Sweden.

Glassman, I. (1959). Metal combustion processes. *American Rocket Society*, 938-959.

Goldstein, J., Echlin, P., and Joy, D. (2007). Scanning electron microscopy and X-ray
microanalysis. 3rd ed. New York: Springer, 21 – 25.

Goodge, J. (2012, March). *Energy-dispersive x-ray spectroscopy (eds)*. Retrieved from
http://serc.carleton.edu/research_education/geochemsheets/eds.html.

Hahma, A., Gany, A., and Palovuori, K. (2006). *Combustion of activated aluminum*.
Department of Chemistry, Faculty of Aerospace Engineering, Technion-Israel Institute of
Technology. Elsevier Inc.

Houim, R., Boyd, E., and Kuo, K. K. (2008). Combustion of aluminum flakes in the post-
flame zone of a hencken burner. *Advancements in Energetic Materials and Chemical
Propulsion.* Edited by Kuo, K. K. and Hori, K., Begell House Inc., New York, pp. 56 –
71, 454-471.

Kuo, K.K., Matthew Sirignano, and Ryan Houim (2010). Ignition and combustion of
energetic particles at ultra-high pressures and heating rates. *DTRA Applied Sciences II
Task Order 0020 Project 3 Kick Off Meeting*, State College, Pennsylvania.

Kumar, D., Fitz-Gerald, J., and Singh, R.K. (1998). Synthesis of high-temperature
superconductive and colossal magnetoresistive surfaces on insulating particles.

Liu, W, K., and Santos, M. B. (1998) *Thin films: Heteroepitaxial systems.* Coston: World Scientific Company, Inc.

Marcus, J. (2002). Analysis: How thermobaric bombs work. *BBC News*. Retrieved from http://news.bbc.co.uk/2/hi/south_asia/1854371.stm.

National. (2008). Retrieved from http://www.nationalterroralert.com/2008/09/29/thermobaric-bombs-al-qaedas-new-weapon-of-terror/.

Ohring, M. (2002). *Material Science of Thin Films*. 2nd ed. Academic Press. Pp. 44-47, 58-97, 128-135, 358.

Orr, P. J., & Kearns, S. L. (2011). X-ray microanalysis of burgess shale and similarly preserved fossils. *Quantifying the Evolution of Early Life*, doi: 10.1007/978-94-007-0680-4_11.

Pulsed Laser Deposition and Epitaxy. (2008). Retrieved from http://www.geocites.com/afserghei/lve.htm/.

Rosenband, V. and Gany. A. (2005) *Activated metal powders as potential energetic materials*, Faculty of Aerospace Engineering, Technion-Israel Institute of Technology, Haifa 3200, Israel

Shachtman, N. (2003) When a gun is more than a gun. *Wired.* Retrieved 15 Sept. 2011 from <http://www.wired.com/politics/law/news/2003/03/58094>

Sirignano, M. (2011). *Modification and implementation of a ballistic compressor to study ignition and combustion of energetic particles at ultra-high pressures and heating rates.* (Master's thesis, The Pennsylvania State University).

Smith, K., and Brenton, B. (2008) "The Scanning electron microscopy." University of Cambridge.

Sutton, G. (2010). *Rocket propulsion elements*. Hoboken, NJ: John Wiley & Sons, Inc.

Swapp, S. (2007). *Scanning electron microscopy (sem)*. Informally published manuscript, Geochemical, University of Wyoming, Wyoming. Retrieved from http://serc.carleton.edu/research_education/geochemsheets/techniques/SEM.html.

Thermobaric weapons. (2003, July). *Second Sight Research*, Retrieved from http://secondsightresearch.tripod.com/id77.html.

TimeDomain CVD, Inc. (2002). *Fundamentals of chemical vapor deposition*. Retrieved from http://www.timedomaincvd.com/CVD_Fundamentals/chemistry/chem_intro.html

UT-Knoxville, (2011, August). *Thin film growth* [PowerPoint slides]. Retrieved from University of Tennessee – Knoxville website: http://web.utk.edu/~prack/Thin%20films/thinfilmgrowth.pdf.

V. Rosenband and A. Gany (2008), Activated metal powders as potential energetic materials, *Advancements in Energetic Materials and Chemical Propulsion*, edited by Kuo, K. K. and Hori, K., Begell House Inc., New York, pp.838-854.

Wildegger-Gaissmaier, A. E. (2003). Aspects of themobaric weaponry. *ADF Health*, *4*(1), Retrieved from http://www.defence.gov.au/health/infocentre/journals/ADFHJ_apr03/ADFHealth_4_1_0 3-06.html

Yagodnikov, D.A., Voronetskii, A. V. (1997), Experimental and theoretical study of the ignition and combustion of an aerosol of encapsulated aluminum particles, *Combustion, Explosives, and Shock Waves* 33 (1): 49-55.

APPENDIX A

PSU BALLISTIC COMPRESSOR PHYSICAL SPECIFICATIONS

Compression Tube

Material	Alloy Steel 4140
Length	3.96 m (156")
Interior Diameter	5.080 cm (2.00")
Interior Volume	8030 cc (490 cu in)
Exterior Diameter	11.326 cm (4.46")

Transition Section

Material	Vasco Max 300
Overall Length	32.56 cm (14.00")
Exterior Diameter	25.40 cm (10.00")
Upstream Diameter	5.080 cm (2.000")
Downstream Diameter	1.270 cm (0.500")
Downstream Length	15.24 cm (6.000")
Upstream Volume	308.90 cc (18.85 cu in)
Downstream Volume	6.60 cc (0.403 cu in)
Overall Volume	315.45 cc (19.25 cu in)

Gas Reservoir

Material	Alloy Steel A515; Stainless Steel 304
Overall Length (Excluding Interior Volume)	1.49 m (58.5")
Overall Length (Including Interior Volume)	2.25 m (88.75")
Exterior Diameter	39.688 cm (15.625")
Approximate Volume of Exterior Volume	0.117 m^3 (7140 cu in)
Approximate Volume of Interior Volume	737 cc (45 cu in)
Interior Diameter of Exterior Volume	35.41 cm (13.94")
Overall Diameter of Interior Volume Pipe	2.13 cm (0.84")

Test Section

Material	Vasco Max C 300
Length (Excluding End Cap Retainer)	14.224 cm (5.600")
Length (Including End Cap Retainer)	21.844 cm (8.600")
Exterior Diameter (Excluding Window Assemblies and Electrodes)	25.400 cm (10.000")
Exterior Diameter (Excluding Window Assemblies and Electrodes)	34.315 cm (13.510")
Interior Volume	8.2 cc (0.5 cu in)

APPENDIX B

PARTICLE HOLDER MODIFICATION TEST DATA

Holder Type	Sample Size	Response
Holder A	0.1011g	Rapid movement of sample in center of holder
	0.3046g	Rapid movement of sample in center of holder, particles escaping surface of mass
	0.5076g	Rapid movement of sample, particles deeper in sample manifesting to top, particles escaping surface of mass
Holder B	0.1012g	Rapid movement of sample in center of holder
	0.3069g	Rapid movement of sample along edge of mass, minimal movement in center of particle mass.
	0.5070g	Rapid movement of sample in an elliptical shape, particles deeper in sample manifesting to top, particles sticking to sides of holder
Holder C	0.1031g	Rapid movement of sample in center of holder
	0.3059g	Rapid movement of sample along edge of mass, particles less concentrated due to flat bottom of holder
	0.5061g	Rapid movement of particles, particles escaping surface of mass above height of holder